Journal of Glaciology (2016), **62**(231) 103–123 doi: 10.1017/jog.2016.16

Densification of layered firn in the ice sheet at Dome Fuji, Antarctica

SHUJI FUJITA,[1,2] KUMIKO GOTO-AZUMA,[1,2] MOTOHIRO HIRABAYASHI,[1] AKIRA HORI,[3] YOSHINORI IIZUKA,[4] YUKO MOTIZUKI,[5] HIDEAKI MOTOYAMA,[1,2] KAZUYA TAKAHASHI[5]

[1]*National Institute of Polar Research, Research Organization of Information and Systems (ROIS) 10-3 Midori-cho, Tachikawa, Tokyo 190-8518, Japan*
[2]*Department of Polar Science, The Graduate University for Advanced Studies (SOKENDAI), 10-3 Midori-cho, Tachikawa, Tokyo 190-8518, Japan*
[3]*Kitami Institute of Technology, Kitami, Japan*
[4]*Institute of Low Temperature Science, Hokkaido University, Sapporo, Japan*
[5]*RIKEN Nishina Center, Wako, Japan*
Correspondence: S. Fujita <sfujita@nipr.ac.jp>

ABSTRACT. In order to better understand the densification of polar firn, firn cores from the three sites within ~10 km of Dome Fuji, Antarctica, were investigated using surrogates of density: dielectric permittivities ε_v and ε_h at microwave frequencies with electrical fields in the vertical and horizontal planes respectively. Dielectric anisotropy $\Delta\varepsilon$ ($=\varepsilon_v - \varepsilon_h$) was then examined as a surrogate of the anisotropic geometry of firn. We find that layered densification is explained as a result of complex effects of two phenomena that commonly occur at the three sites. Basically, layers with initially smaller density and smaller geometrical anisotropy deform preferentially throughout the densification process due to textural effects. Second, layers having a higher concentration of Cl^- ions deform preferentially during a limited period from the near surface depths until smoothing out of layered Cl^- ions by diffusion. We hypothesize that Cl^- ions dissociated from sea salts soften firn due to modulation of dislocation movement. Moreover, firn differs markedly across the three sites in terms of strength of geometrical anisotropy, mean rate of densification and density fluctuation. We hypothesize that these differences are caused by textural effects resulting from differences in depositional conditions within various spatial scales.

KEYWORDS: antarctic glaciology, glacial rheology, ice core, ice physics, polar firn

1. INTRODUCTION

Understanding the evolution of firn in polar ice sheets is fundamental to better understand ice core gas signals and data of microwave remote sensing. Metamorphism and initial layering of snow is known to be dependent on various surface conditions, such as the accumulation rate, temperature, temperature gradient and mechanical forcing by wind (e.g. Colbeck, 1989; Dang and others, 1997; Craven and Allison, 1998; Cuffey and Paterson, 2010; Sugiyama and others, 2012). After the initial processes of firn formation at the surface of the ice sheet, firn subsequently undergoes various further processes of both metamorphism and deformation with both increasing time and depth. Such processes, including initial fractures, rearrangement of ice grains, creep deformation, pressure sintering with shrinkage of either pore spaces or closed air bubbles and grain growth, are complex (e.g. Bader, 1939; Benson, 1962; Anderson and Benson, 1963; Gow, 1968, 1975; Maeno and Ebinuma, 1983; Alley, 1988; Hondoh, 2000; Fujita and others, 2009, 2014; Kipfstuhl and others, 2009; Cuffey and Paterson, 2010; Hörhold and others, 2011, 2012; Lomonaco and others, 2011).

Based on studies of very deep ice cores, Bender (2002) discovered that the orbital tuning chronology for the Vostok climate record was supported by trapped gas composition, such as the gas fractionation ratio of O_2/N_2 (O_2/N_2 ratio) and total air content (TAC). Subsequently, it has been demonstrated that both O_2/N_2 ratio and TAC are empirically correlated with orbital changes of the local summer insolation in the other ice cores both from Antarctica (e.g. Kawamura and others, 2007; Raynaud and others, 2007; Suwa and Bender, 2008b; Landais and others, 2012) and Greenland (Suwa and Bender, 2008a). As time markers of very deep ice cores, a 2σ uncertainty of O_2/N_2 ratio and TAC represent 2 ka and 6 ka respectively (e.g. Kawamura and others, 2007; Bazin and others, 2012). Because of the importance of the O_2/N_2 ratio and TAC as time markers in ice core studies, the original discovery by Bender stimulated recent studies of polar firn. It has been suggested that the empirical correlation between the orbital changes of the local summer insolation and the trapped gas composition is metamorphism that occurs at the surface of the ice sheets (e.g. Bender, 2002; Kawamura and others, 2004, 2007; Fujita and others, 2009, 2014; Hutterli and others, 2009). Insolation-sensitive microstructure appears to be preserved within layers of firn metamorphism up until pore close-off. Despite recent advances, a number of important questions remain unanswered. Several studies have found that firn with initially lower density becomes denser than firn with initially higher density, thereby creating a local convergence of density fluctuations in the density range, 580–650 kg m^{-3} (e.g. Gerland and others, 1999; Freitag and others, 2004; Fujita and others, 2009, 2014; Hörhold and others, 2011). For the Dome Fuji (DF)

Antarctic ice core from an elevation of 3,800 m, Fujita and others (2009) suggested that the summer insolation caused textural effects such as ice–ice bonding, additional clustering of c-axes around the vertical, and anisotropic geometry of ice and pore spaces. They hypothesized that the strength of these textual effects determines the duration for firn-to-ice transition and so determines the degree of lower O_2/N_2 ratio and smaller TAC.

Impurity ions have also been suggested to be relevant to firn evolution. The correlation between deformation and some ions such as Ca^{2+} (Hörhold and others, 2012; Freitag and others, 2013) was empirically discovered at sites in Greenland and at some sites in Antarctica with elevations lower than ~3,000 m. More recently, based on analysis of the firn core from the North Greenland Eemian Ice Drilling (NEEM) camp in North Greenland, Fujita and others (2014) found that layers with more F^- and Cl^- and some cations deposited between the autumn and the subsequent summer, deform preferentially during all densification stages from the near surface depths until pore close-off. Fujita and others (2014) suggested that the layered enhancement of deformation is partly a result of textural effects initially formed by the seasonal variation of metamorphism and partly a result of ions such as F^-, Cl^- and NH_4^+, which are known to modulate dislocation movement in the ice crystal lattice. They further hypothesized that high correlations between Ca^{2+} ions (and Mg^{2+} and Na^+) and deformation are superficially caused by the seasonal synchronicity with cycles of F^-, Cl^- and NH_4^+ and the seasonal variation of metamorphism.

Considering the above background, and as summarized in Table A8, no studies have examined how the abovementioned ions are related to layered deformation in Antarctic Dome summit sites at elevations above ~3,000 m. In the present study, we consider the following: (1) Can we observe significant correlations between ions such as F^-, Cl^- and/or NH_4^+ and the layered enhancement of deformation, like the Greenland NEEM case? (2) If so, how are such effects related to previously proposed hypotheses of the textural effects? (3) Is there spatial variability in the nature of firn evolution? This question arises because both depositional- and subglacial-conditions are highly spatially variable, even around the DF summit (e.g. Fujita and others, 2011, 2012). (4) How do metamorphism and initial layering of snow influence densification processes in general? In order to explore these questions, we investigated three ~120-m-long firn cores taken from three DF sites (Fig. 1). As in recent studies (Fujita and others, 2009, 2014), we investigated the tensorial values of the dielectric permittivity, density, major ions and water stable isotope ratios, and their magnitudes, fluctuations and mutual correlations.

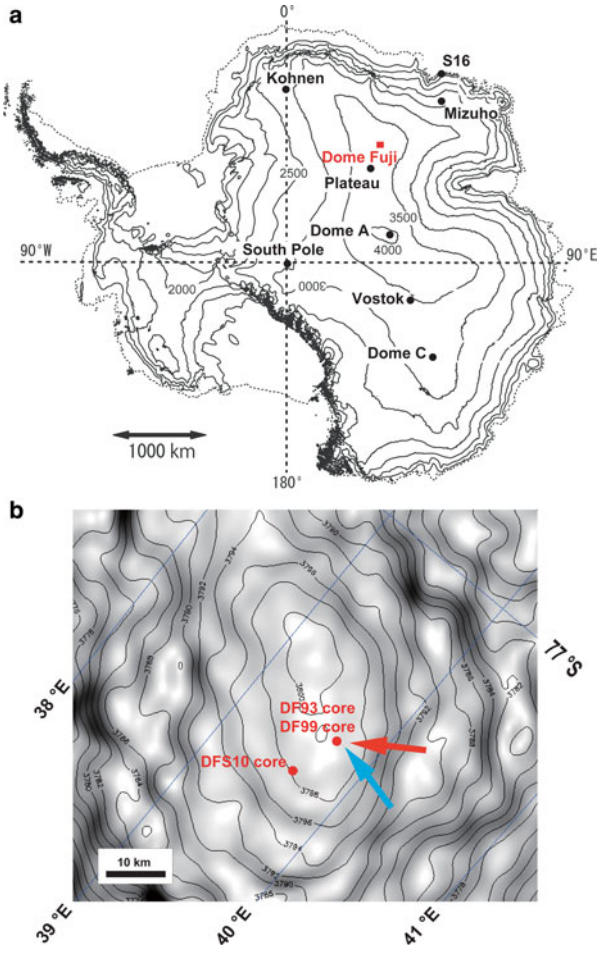

Fig. 1. Map of the study sites. (a) DF in Antarctica. (b) Location of the three sites near DF. The rectangular area in (b) is the same as the area indicated in red in (a). Distance between site DF93 and site DF99 is 100 m. Site DFS10 is located ~10 km south-southwest of the other two sites on the leeward side of the prevailing winds. The blue and red arrows are the annual mean direction of the wind and the center direction of the wind in the strong wind events, respectively (Fujita and others, 2011). The elevation contour map in (a) and (b) is based on the DEM (Bamber and others, 2009). Gray shading in the map (b) indicates the steepness of the surface slope.

2. METHOD OF MEASUREMENT AND SAMPLES

2.1. Dielectric permittivity measurement and samples

Table 1 provides a list showing characteristics of the measurement methodology used to examine the DF firn cores. The dielectric permittivity tensor was measured as a surrogate of density and vertical elongation of ice and pore spaces within firn, as described in previous studies (Fujita and others, 2009, 2014 and references therein). It is well accepted that the dielectric permittivity of ice, firn and snow at high frequencies such as short radiowave (MHz) and microwave (GHz) ranges under the temperature range of the cryosphere is primarily dependent on density. Earlier studies (e.g. Evans, 1965; Sihvola and Kong, 1988; Lytle and Jezek, 1994) have shown that structural anisotropy of snow grains and pore spaces is associated with anisotropic dielectric properties. In this study, dielectric permittivities ε_v and ε_h at microwave frequencies with electrical fields in the vertical and horizontal planes, respectively, were measured simultaneously with a resolution of ~22 mm (diameter) and a depth increment of 5 mm. Here, ε_h is a density surrogate, without effects of the vertically elongated geometry of pore space and ice. The dielectric anisotropy $\Delta\varepsilon$ ($=\varepsilon_v - \varepsilon_h$) is then examined as a surrogate for the anisotropic geometry of ice and pore spaces within the microstructure. Note that, Fujita and others (2009; Fig. 7) investigated the applicability of $\Delta\varepsilon$ as an indicator of structural anisotropy in the DF firn. The axial ratio, an indicator of structural anisotropy, was calculated for the 23 X-ray absorption microtomography measurements. The axial ratio was positively correlated with $\Delta\varepsilon$. Despite data scatter caused by different sampling portions and different sampling sizes used (~22 mm in diameter and ~7 mm in thickness for the dielectric permittivity

Table 1. Characteristics of the measurement methodology used to examine the DF firn cores in the present study

ID	Method or item and laboratory	Target properties	Continuous/Spot? Resolution in Depth	Shape and size of the sample[a]	Cores measured
1	Dielectric permittivity tensor measurement using an open resonator method at NIPR	Dielectric permittivity along the vertical and horizontal, ε_v and ε_h; dielectric anisotropy, $\Delta\varepsilon = \varepsilon_v - \varepsilon_h$	Continuous 22 mm	Slab $\Delta x = 5$ mm, $\Delta y = 60$ mm, $\Delta z = 500$ mm	DF93, DF99 and DFS10 (see Fig. 2)
2	Major ions measured at NIPR	Cations (Na^+, K^+, Mg^{2+}, Ca^{2+} and NH_4^+) and anions (Cl^-, SO_4^{2-}, NO_3^-, F^- and several other anions)	Continuous 20 mm	Sliced with $\Delta z = 20$ mm	DF93, DF99 and DFS10 (Fig. 2; Table 1)
3	Major ions of DF99 core measured at ILTS	Cations (Na^+, K^+, Mg^{2+} and Ca^{2+}) and anions (Cl^-, SO_4^{2-}, NO_3^- and several other anions). F^- anions were unavailable. NH_4^+ anions were available in a limited (71.4–71.8 m) sample.	Continuous Ultra-high resolution of 2–4 mm	Sliced with $\Delta z = 2$–4 mm	DF99 core with four depth ranges of 6.1–6.4 m, 17.3–17.6 m, 40.9–41.2 m and 71.4–71.8 m
4	Major ions of DFS10 core measured at RIKEN	Cations (Na^+, K^+, Mg^{2+} and NH_4^+) and Anions (Cl^- and SO_4^{2-}). F^- anions and Ca^{2+} cations were unavailable.	Continuous 50 mm at 0–20 m 40 mm at 20–50 m 30 mm at 50–80 m 25 mm at 80–83 m	Sliced with $\Delta z = 20$–40 mm	DFS10 core
5	Water isotope ratios at NIPR	Oxygen isotope ratio and hydrogen isotope ratio	Continuous 20 mm	Sliced with $\Delta z = 20$ mm	Same as ID 2
6	Density measurement using the X-ray transmission method at ILTS	Bulk density, ρ	Continuous 1 mm	Slab $\Delta x = 25$ mm, $\Delta y = 60$ mm, $\Delta z = 500$ mm	Same as ID 3
7	Density measurement using the gamma-ray transmission method at NIPR	Bulk density, ρ	Continuous 3.3 mm	Slab $\Delta x = 25$ mm, $\Delta y = 60$ mm, $\Delta z = 500$ mm	DF99 core at a depth of 71.4–71.8 m

[a]Δx, Δy and Δz are sample dimensions along the horizontal axis, orthogonal axis in the horizontal and the vertical, respectively.

measurements and 15 mm ϕ cylinder with 15 mm thickness for the X-ray absorption microtomography measurements), the positive correlation between $\Delta\varepsilon$ and the average axial ratio for each sample was observed. The data are in line with the earlier studies as mentioned above, and hence, we can use $\Delta\varepsilon$ as an indicator of structural anisotropy. We investigated $\Delta\varepsilon$ to better understand several aspects, as listed below (see Fujita and others, 2009).

(1) Dielectric anisotropy, $\Delta\varepsilon$ is hypothesized to indicate the degree of metamorphism, attained by vertical movement of moisture at the ice sheet surface, forming the vertically elongated features of the ice matrix and pore spaces.
(2) Firn with higher/lower $\Delta\varepsilon$ is hypothesized to indicate the presence of less/more deformable firn.
(3) Firn with higher $\Delta\varepsilon$ potentially means the vertically elongated shape of pore spaces may play some role in the vertical diffusivity of gas through the channels of open pores in the bubble close-off zone.

Fujita and others (2009) investigated the applicability of $\Delta\varepsilon$ as an indicator of structural anisotropy in the Dome Fuji firn (see their figure 7). The axial ratio, an indicator of structural anisotropy, was calculated for the 23 X-ray absorption microtomography measurements. The axial ratio was positively correlated with $\Delta\varepsilon$. Despite data scatter caused by different sampling portions and different sampling sizes used (~22 mm in diameter and ~7 mm in thickness for the dielectric permittivity measurements and 15 mm Φ cylinder with 15 mm thickness for the X-ray absorption microtomography measurements), the positive correlation between $\Delta\varepsilon$ and the average axial ratio for each sample was observed. The data are in line with the earlier studies as mentioned above, and hence, we can use $\Delta\varepsilon$ as an indicator of structural anisotropy.

An open resonator designed for frequencies of 26.5–40 GHz was used. Slab-shaped firn samples, thickness ~5–7 mm and width, 60 mm, in width were scanned within an electrical field of microwave resonance. All our dielectric permittivity measurements were performed in the frequency range of 33–35 GHz and under the temperature range −16 ± 1.5°C at the National Institute of Polar Research (NIPR), Japan. The errors associated with sample thickness variations (<0.1 mm) were minimized by solving equations (Jones, 1976; Komiyama, 1991) for multiple resonant frequencies simultaneously, to find a unique solution of dielectric permittivity with a common sample thickness. The final errors in permittivity and dielectric anisotropy $\Delta\varepsilon$ ($=\varepsilon_v - \varepsilon_h$) were ±0.005 and ±0.001 respectively. The errors in $\Delta\varepsilon$ were markedly smaller than the permittivity errors due to the physical principle of the simultaneous measurement of the difference of the two resonant frequencies (Matsuoka and others, 1997).

Samples were taken from the three sites near DF. Basic information is listed in Table 2. Site DF93 is the firn core from the pilot hole for the very deep ice core (Watanabe and others, 2003). The 112 m core was preserved at a temperature of −50°C at the Institute of Low Temperature Science (ILTS), Hokkaido University, Japan. The basic physical properties of this core have been published (Watanabe and others, 1997; Hori and others, 1999). The dielectric permittivity tensor was first measured in 2002–2003 and published by Fujita and others (2009). In the previous study, 10 portions of ~0.5-m-long samples or shorter were used. In the present study, 137 additional sample portions were used, covering 55.7 m sections within the 112 m core. The available depth portions used for this study are shown in Figure 2 as ID 1.

Site DF99 is located just 100 m south of the DF93 borehole. A 108-m core was drilled in 1999. Again, the cores were preserved at a temperature of −50°C at ILTS. From the

Table 2. Information of sampling sites, glaciological conditions and analysis

Core site name	DF93	DF99	DFS10
Latitude (°)	−77.316	−77.318	−77.395
Longitude (°)	39.703	39.704	39.617
Elevation (m)	3800	3800	3790
Ice thickness (m)	3028 (±15)	Unknown	2950 (±50)
Annual accumulation	25.5 (±0.2) (kg m^{-2})[a]	98.9% (±0.2%) of DF93[b]	96.7% (±0.2%) of DF93[b]
Annual mean air temperature (°C)	−54.3	Same as DF93	No data
10 m snow temperature (°C)	−57.3	Same as DF93	No data
Annual mean wind speed	5.9 at 10 m	Same as DF93	No data
Core length (m)	112	108	122
Year of ice coring	1993	1999	2010
Year of analyses for the present study	2002–2014	2013–2014	2012–2014
Note	DF Station	100 m south of the DF93 hole	Leeward side of DF

[a]From 1260 to present (Igarashi and others, 2011).
[b]Derived based on volcanic synchronization with the DF93 core for the period from 1260 to present.

whole cores, 22 samples of ~0.5 m or shorter were used. As a result, the measurements covered a 9.2 m section of the core. The measurements of the present study were performed in 2013 and 2014. The annual accumulation rate at site DF99 is 98.9% (±0.2%) of that at site DF93 based on volcanic synchronization and density measurements (Table 2).

Site DFS10 is located on the leeward side of DF, ~10 km from sites DF93 and DF99 (Fig. 1b). In the DF area, the prevailing wind is between NE and E (e.g. Kameda and others, 1997; Fujita and others, 2011). The core was drilled in 2010 and preserved at a temperature of −50°C at NIPR. The measurements were performed in 2012–2014. From the near surface depths to a depth of 114 m, 261 samples of ~0.5 m long or shorter were measured from a 101.0 m core. The annual accumulation rate at site DFS10 is 96.7% (±0.2%) of that at site DF93, based on volcanic synchronization and density measurements (Table 2).

2.2. Analysis of major ions and water isotope ratio

Major ions were measured at three different laboratories using different instruments and different spatial resolutions. At NIPR, for each of the DF93, DF99 and DFS10 cores, five selected portions at the same depth range, from 71 to 92 m, were measured with a resolution of 20 mm (IDs 2 and 5 in Table 1 and Fig. 2). Near DF, the pore close-off depth has been estimated to be ~104 m (Watanabe and others, 1997). Bubble formation occurs gradually within ~20 m before pore close-off (e.g. Watanabe and others, 1997; Fujita and others, 2009). Thus, these data from the three sites are useful for comparing three cores at the same depth range just before pore close-off; the nature of the firn at this depth is expected be directly linked to air-enclosure precesses. We sliced 3 mm of firn from the outside of the section in order to decontaminate the surface. This was done on a clean bench in a cold room using a clean ceramic knife. The cleaned firn section was then sliced at depth intervals of 20 mm, and each sliced fraction was sealed in a clean polyethylene bag. At NIPR, the DX500 (Dionex) ion chromatography system was used to measure the cations (Na^+, K^+, Mg^{2+}, Ca^{2+} and NH_4^+) and anions (Cl^-, SO_4^{2-}, NO_3^-, F^- and several others), and the instrument used to measure oxygen isotope ratios was a Delta V mass spectrometer (Thermo Fisher Scientific). For each core of DF93, DF99 and DFS10, ~120 measurements were performed, covering a depth of 2.4 m.

Four sets of ultra-high resolution data were produced for major ions from limited depths in the DF99 core. The depth ranges were 6.1–6.4 m, 17.3–17.6 m, 40.9–41.2 m and 71.4–71.8 m as shown in Figure 2 (IDs 3 and 6). The measurements were performed at ILTS. The method of

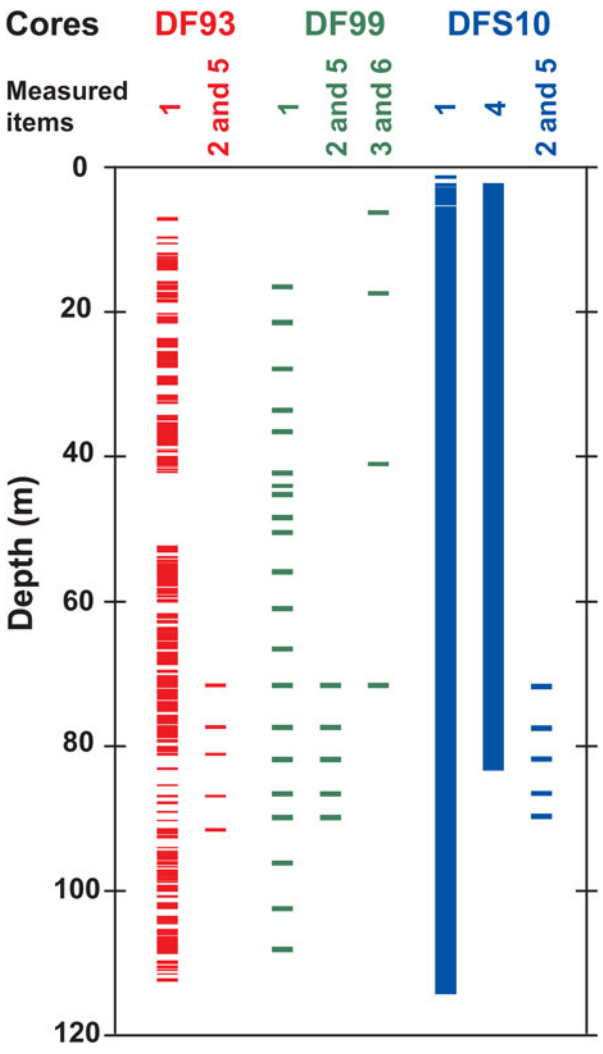

Fig. 2. Depth portions of the firn cores used for each item of measurement. For each core of DF93, DF99 and DFS10, measured items are indicated by ID numbers that are listed in Table 1. Marker symbols indicate depths covered for each measurement.

sample preparation was basically the same as that used at NIPR, except that sample slicing was performed at depth intervals from 2 to 4 mm. The estimated thickness error of each sample was <0.5 mm. The analytical procedures were approximately the same as in previous studies by Iizuka and others (2004b, 2006). At ILTS, a DX500 (Dionex) ion chromatography system was also used to measure the cations (Na^+, K^+, Mg^{2+}, Ca^{2+} and NH_4^+) and anions (Cl^-, SO_4^{2-}, NO_3^- and several others). F^- anions were not measured. The concentration of soluble ions was measured with an estimated error of <5% (Igarashi and others, 1998). For these four sets of samples, dielectric permittivity measurements were not available. However, continuous density profile data using X-ray transmission (Hori and others, 1999) were available. The spatial resolution of the density profile was ~1 mm. In addition, for a portion of samples, a high-precision gamma-ray density meter (Nanogray Inc. model PH-1100, http://www.nanogray.co.jp/products/) (Miyashita, 2008) was used to determine density at 3.3 mm resolution.

For the DFS10 core, there is a dataset of major ions that continuously covers the area from the near surface depths to a depth of 83 m with resolutions ranging from 50 to 25 mm, shown as ID 4 in Figure 2 and Table 1. This dataset was established at RIKEN using a Dionex ICS2000 ion chromatography system. In the present study, we examined the data for cations (Na^+, K^+, Mg^{2+} and NH_4^+) and anions (Cl^- and SO_4^{2-}). Note that, no continuous data of Ca^{2+} or water isotope ratio were available for this study.

2.3. Relation between the measured dimension of firn and the target properties

The range of depth resolutions for our measurements was in most cases from 22 to 1 mm (measurement IDs 1–6 except ID 4 in Table 1). Here, annual accumulation rate at the three sites are ~25 kg m^{-2}. For our firn density of 300–830 kg m^{-3}, average annual layer thickness ranges from 83 to 30 mm. Thus, depth resolution of our measurement is in most cases finer than annual layer thickness. In the case of measurement ID 4 (major ions measured for the DFS10 core), depth resolutions at each depth range (Table 1) are still always finer than annual layer thickness. In addition, we used 0.5 m (or shorter) samples for each series of continuous measurements. This length contains ~6–17 annual layers or less in a sample.

3. RESULTS

3.1. Evolution of ε_h vs depth

The data for the dielectric permittivity (ε_h and ε_v) vs depth for the three cores are shown in Figure 3. We verified that ε_v was always larger than ε_h by rotating the electrical field within the samples in the resonator. $\Delta\varepsilon$ ($=\varepsilon_v - \varepsilon_h$) is shown later in Figures 5, 6. Figure 4 shows the values of ε_h for the three cores. Note that the three cores have approximately the same depth-density profiles, with small but significant differences among them. The DF93 core has the largest ε_h values, and thus the largest density values, as highlighted in Figure 4b. The DFS10 core is approximately as dense as the DF93 core at depths between 50 and 100 m. However, at depths from the near-surface to ~50 m, the DFS10 core is significantly less dense than the DF93 core. The DF99 core tends to be less dense than the other two cores. At depths of between 50 and 100 m, ε_h for the DF99 core is up to 0.02 smaller than that for the DF93 core, which is equivalent to a difference in density of approximately 9 kg m^{-3}. Considering the uncertainty of the single measurement of permittivity, ±0.005, the smaller values of ε_h for the DF99 core, compared with the DF93 and DFS10 cores, are significant. The scale of density ρ (kg m^{-3}) equivalent to ε_h at the measurement temperature (Fujita and others, 2014) is indicated along the right-hand axis of Figure 4 as a reference.

3.2. Evolution of $\Delta\varepsilon$ vs depth

The $\Delta\varepsilon$ vs depth data are shown in Figure 5. In the figure, raw data points, mean values within ~0.5 m samples, and the average tendency along the entire depth range are given. A

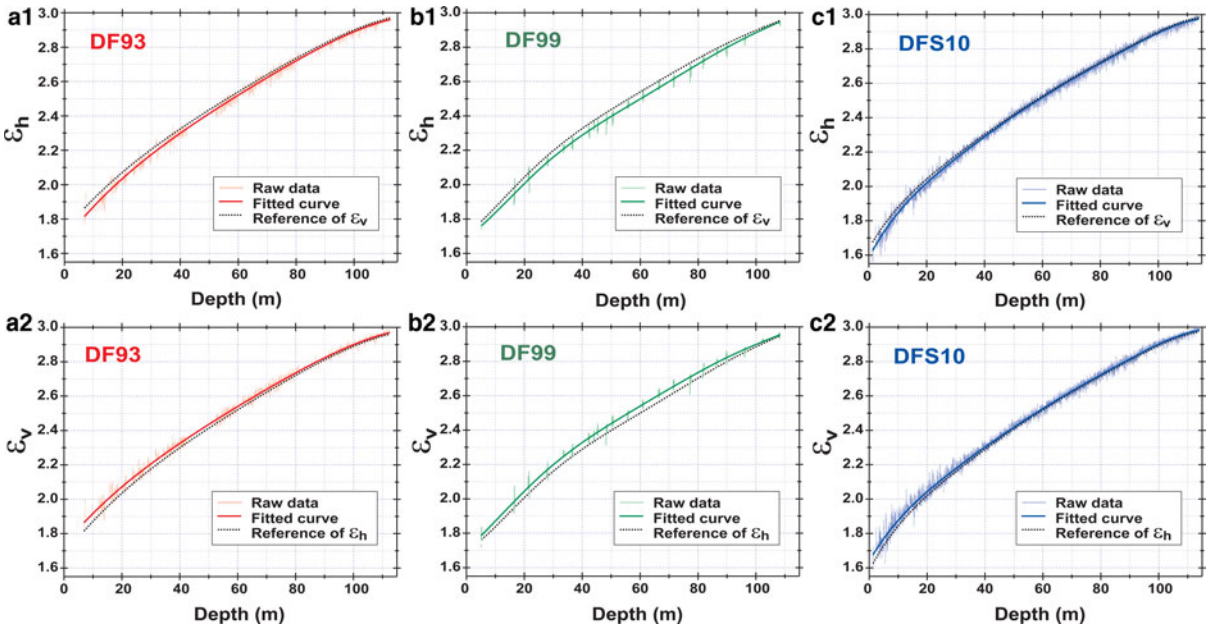

Fig. 3. Dielectric permittivity in the vertical plane (ε_v) (Panels a1, b1, c1) and in the horizontal plane (ε_h) (Panels a2, b2, c2) for the three firn cores. The data from the DF93, DF99 and DFS10 cores are indicated in red, green and blue in (a), (b) and (c), respectively. In Figures 4 through 8 and 15 below, the colors of lines and markers are consistent between figures.

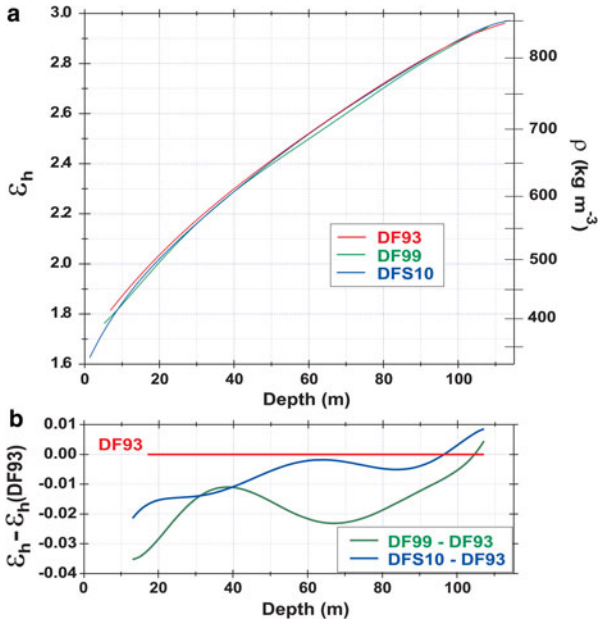

Fig. 4. (a) Polynomial fitting curves for ε_h (values shown on the left axis) for the three firn cores. The right vertical axis shows the reference scale for density ρ (kg m^{-3}) empirically converted from ε_h (Fujita and others, 2014). (b) Values of the ε_h curves for the DF99 core (green) and the DFS10 core (blue) are expressed as the difference from the ε_h values of the DF93 core, to highlight the difference between them. The uncertainty of these differences is 0.07. The DF93 core has the largest ε_h values among the three cores, and the DFS10 core has the second largest ε_h values. The DF99 core tends to be less dense than the other two cores. The ε_h values for the DF99 core (green) and the DFS10 core (blue) catch up with ε_h values for the DF93 core only near the pore close-off depth (95–115 m).

remarkable feature is that the size and trend of $\Delta\varepsilon$ differ clearly and significantly across the three sites. Preliminary $\Delta\varepsilon$ data from DF93 were previously reported by Fujita and others (2009). A number of additional data in the present study agree well with those previous data (Fig. 5a), confirming the absence of detectable deterioration of samples during a 10-year period. We confirm that $\Delta\varepsilon$ decreases only gradually with increasing density, with remarkable fluctuations across only slightly different depths. Unlike the Greenland NEEM core (Fujita and others, 2014), no features of $\Delta\varepsilon$ bending at a density of ~600 kg m^{-3} or at a ε_h of ~2.2 are observable (see Fig. 15). This density and the value of ε_h occur at a depth of ~40 m in the three cores near DF. In the DF99 core (Fig. 5b), $\Delta\varepsilon$ exhibit significant scatter from ~0.01 to 0.08 within a depth range down to ~90 m, below which, $\Delta\varepsilon$ decreases. Considering that site DF99 is located ~100 m south of site DF93, $\Delta\varepsilon$ at site DF99 is surprisingly large. Moreover, $\Delta\varepsilon$ at site DFS10 is different from those at the other two sites and decreases steeply and smoothly from the near surface depths to greater depths (Fig. 5c). The mean values within each approximately 0.5 m section have smaller fluctuations than those of DF93 or DF99. A number of data points have values as small as zero at a depth range of 40–90 m, i.e. the firn over some sections within the data is geometrically isotropic in terms of dielectric permittivity values. Another feature is that there is a broad minimum of $\Delta\varepsilon$ at depths of ~80 m, where $\Delta\varepsilon$ is as small as ~0.007. At depths below this local minimum, $\Delta\varepsilon$ gradually increases again. This gradual increase in $\Delta\varepsilon$ is explained by the gradual increase in the cluster strength of *c*-axis around the vertical (Fujita and others, 2009). $\Delta\varepsilon$ is a surrogate for the anisotropic geometry within the microstructure. However, when the anisotropic geometry is weak or absent with $\Delta\varepsilon$ being <~0.01, $\Delta\varepsilon$ generated as a result of crystal orientation fabrics can appear.

3.3. Evolution of the relation between $\Delta\varepsilon$ and ε_h

The data in Figures 3 (ε_h-*z* plots; here *z* is depth) and 5 ($\Delta\varepsilon$-*z* plots) are expressed as $\Delta\varepsilon$–ε_h plots in Figure 6, to determine the correlation between the degree of geometrical anisotropy and density. Basically, the large-scale variation of $\Delta\varepsilon$ is gradual and smooth, with the exception of a rapid ε_h decrease at ~2.85 near DF99. This value of ε_h is slightly lower than that at the firn-to-ice transition (ε_h of 2.91 is

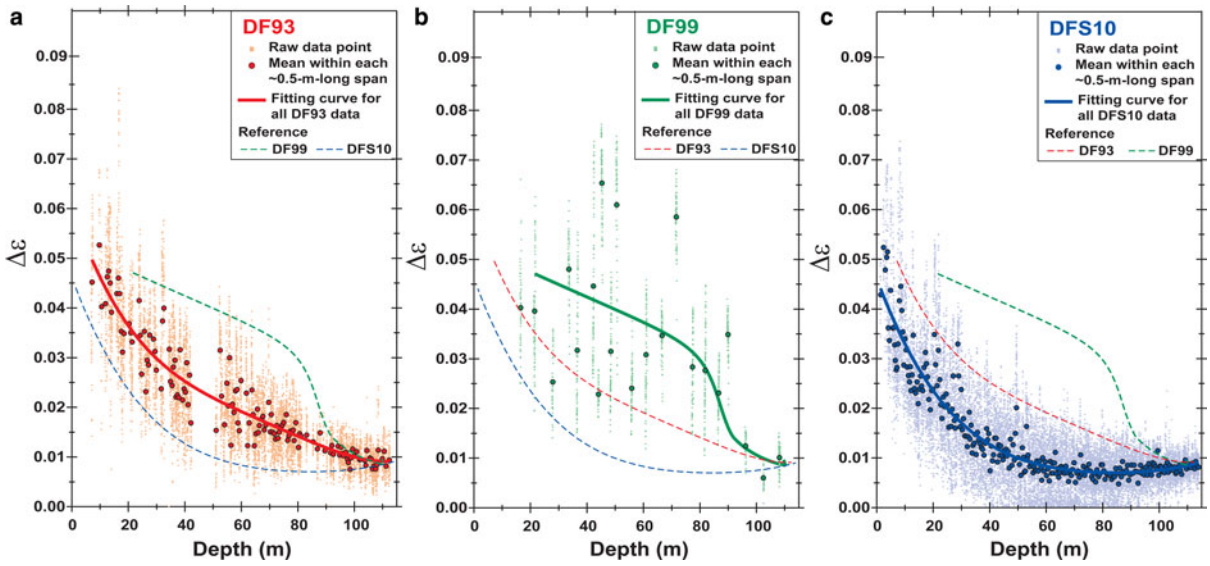

Fig. 5. Dielectric anisotropy ($\Delta\varepsilon = \varepsilon_v - \varepsilon_h$) for the three firn cores. Data for the DF93, DF99 and DFS10 cores are presented in (a), (b) and (c), respectively. In each figure, raw data points, the average value within each ~0.5-m-long sample, and a fitting curve for all data points are shown. The DF99 core has markedly large values of $\Delta\varepsilon$. The DFS10 core has the smallest values among the three cores. In addition, only the DFS10 core has a broad local minimum at ~80 m.

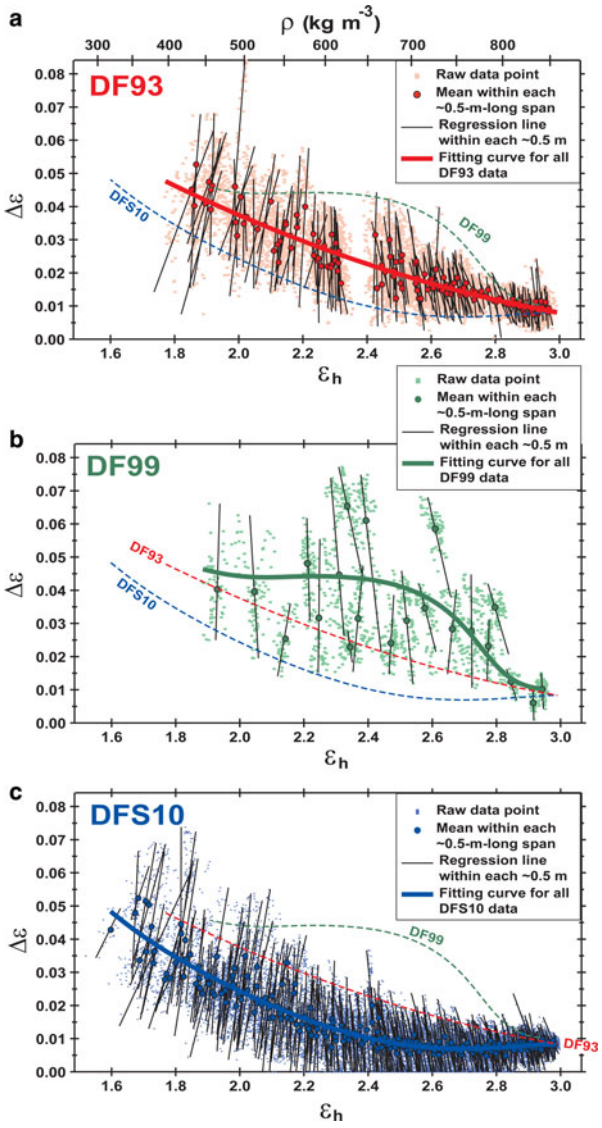

Fig. 6. Plot of $\Delta\varepsilon$ vs ε_h for the three firn cores. In each figure, raw data points, average values within each ~0.5 m sample, a regression line within each sample, and a fitting curve for the entire dataset are shown. Note that each ~0.5 m sample contains ~6–17 annual layers. Commonly, positive correlations in shallower depths change into negative correlations at greater depths.

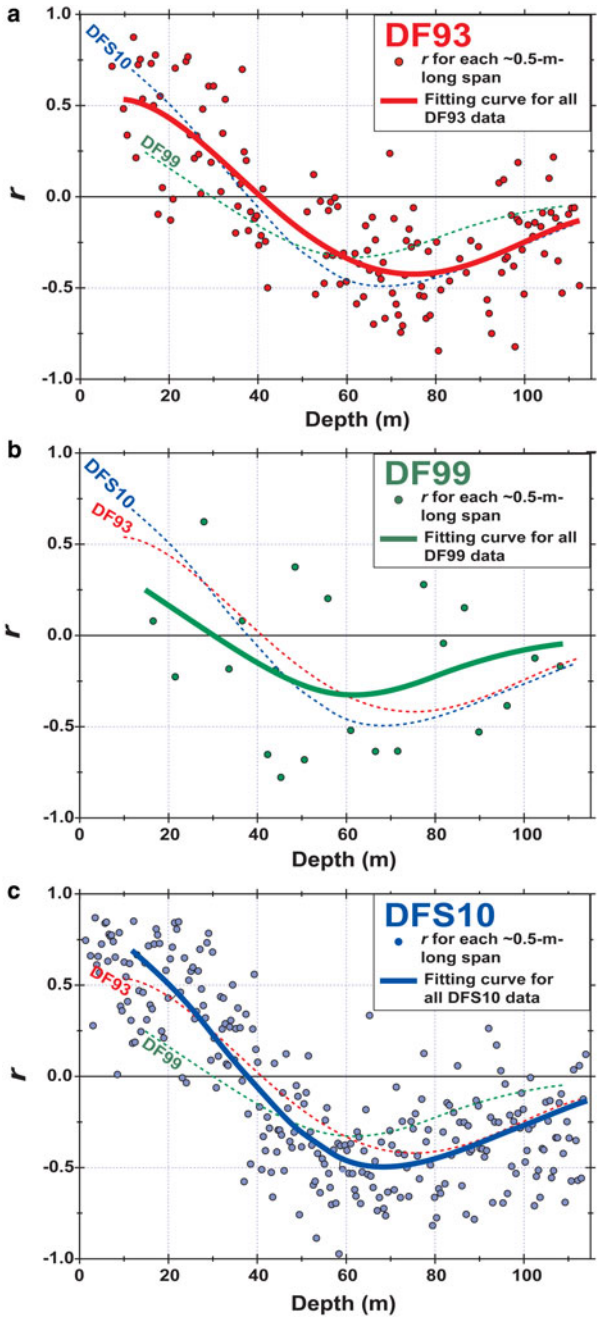

Fig. 7. Linear correlation coefficients between $\Delta\varepsilon$ and ε_h for each ~0.5 m sample (containing ~6–17 annual layers or less) of the three firn cores. In each panel, data points of linear correlation coefficients (r) and a fitting curve for the depth-dependent tendency are given. In each panel, fitting curves of the two other cores are shown for reference purposes. Commonly, for the three cores, r reaches zero near ~40 m, and becomes negative at greater depths. The negative correlations have broad minima at 60–70 m. Below these depths, r approaches zero. In case of the DF region, the large-scale variation of r is basically caused by textural effects and not by softening/hardening effects associated with ions.

equivalent to a density ρ of 830 kg m^{-3}). We also reconfirm that the correlation between $\Delta\varepsilon$ and ε_h changes from positive to negative, as shown by the gradient of the regression lines for several ~0.5-m-long samples (Fujita and others, 2009). Here, we verify that this feature is robust at all the three sites through several additional measurements. This feature is further shown in Figure 7 as the linear correlation coefficients (r) between $\Delta\varepsilon$ and ε_h vs depth. In Figure 7, we observe that r is positive near the ice sheet surface at all the three sites. Moreover, r becomes zero at ~40 m, where ε_h is 2.3, and thus ρ is 610 kg m^{-3}. Below this depth range, r has broad minima at depths between 60 and 80 m, and r approaches zero at a depth of ~120 m. The scattering of r is higher at DF99 (Fig. 7b) than at DF93 and DFS10 (Figs 7a and c).

3.4. Fluctuation of ε_h vs depth

Fluctuations of ε_h were calculated for each of the ~0.5-m-long samples. The standard deviation of ε_h is expressed as σ_h, as shown in Figure 8. Commonly for the three sites, σ_h have local minima at depths of ~40 m. This common depth of the local minima agrees with the depth of the zero value of r. At three sites, σ_h have broad local maxima at depths of 60–90 m. Note that σ_h reflects the fluctuation of density. This type of density behavior was referred to as density crossover or local convergence of density (e.g. Gerland and others, 1999; Freitag and others, 2004; Fujita and others, 2009; Hörhold and others, 2011, 2012). The size of σ_h

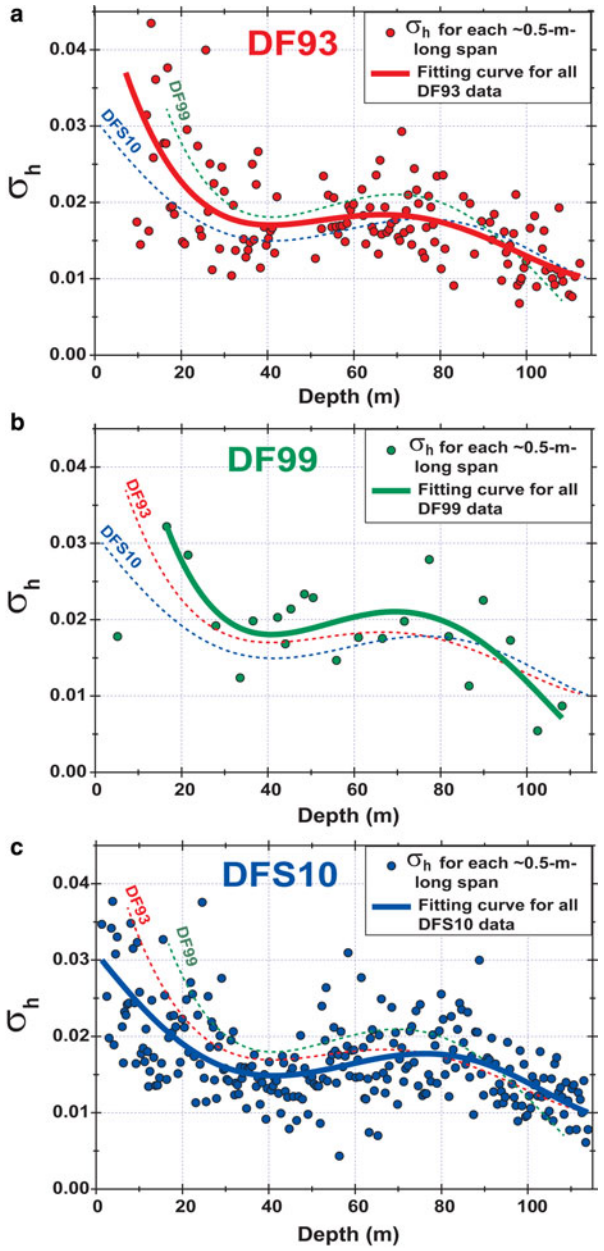

Fig. 8. Standard deviation of ε_h for each ~0.5 m sample (containing ~6–17 annual layers or less) of the three firn cores. In each figure, data points of the standard deviation (σ_h) and a fitting curve for the entire depth are given. In each panel, fitting curves of the two other cores are shown for reference purposes. Commonly, for the three cores, there are local minima of σ_h at depths of ~40 m. In addition, there are broad local maxima at ~70 m. Below the local maxima, σ_h decreases monotonically. In the case of the DF region, the presence of local minima and maxima of σ_h is basically a result of textural effects, rather than the softening/hardening effects of ions. See the text for details.

differs among the three sites. Although there are depth-dependent variations, the size of σ_h increases in the order of DF99, DF93 and DFS10.

3.5. Major ions

3.5.1. Major ions in the three cores in the depth range just before pore close-off (71–92 m)

In Table 4, we list statistics for the concentration of major ions, dielectric permittivity and water stable isotope ratios, from five depth ranges from 71 to 92 m, as listed in Table 3. These data of major ions are also shown in Figure 9. Among the investigated major ions, SO_4^{2-}, Cl^- and Na^+ have high concentrations (25–100 ppb). NH_4^+ and NO_3^- concentrations are also relatively high (10–35 ppb). The concentrations of F^- are very small, on the order of 0.1 ppb. We also note that at the three sites, the ranges of ion concentrations are approximately the same. In addition, we confirm that in the DFS10 core (ID 4 in Fig. 2, Table 1), the ranges of ion concentrations are approximately the same in the entire depth range from the near surface depths to about 83 m (data not shown).

Next, the correlation between the physical layering (ε_h and $\Delta\varepsilon$) and chemical layering was investigated in this depth range just above pore close-off (and later for the other depth ranges, too). The linear correlation coefficients r are listed in Table 5. Moreover, r values between the logarithmic values of ion concentrations vs deviatoric ε_h (deviation from the average tendency) and $\Delta\varepsilon$ are shown in Figure 10. Logarithmic values of ion concentrations are used here under the assumption that the deformation is most likely related to the logarithm of the ionic concentrations (e.g. Jones, 1967). Here, we document the major features appearing in Figure 10 and Table 5. Note however, that the major features are valid for the 71–92 m depth interval and not for the intervals measured at shallower depths of the DF99 and DFS10 core, as discussed later.

(1) With ε_h, ions Na^+, Mg^{2+} and SO_4^{2-} have large and significant positive correlations with r of 0.4–0.7.
(2) With ε_h, some other ions, namely, Cl^-, Ca^{2+} and K^+, are more weakly positively correlated with r by up to 0.5.
(3) With ε_h, NH_4^+ tends to be negatively correlated with r by up to −0.4.
(4) The other ions such as F^- or NO_3^+ show no consistent correlations with ε_h.
(5) With $\Delta\varepsilon$, NH_4^+, Ca^{2+} and K^+ tend to be positively correlated with r by up to +0.5.
(6) The other ions appear to have no consistent correlation tendency with $\Delta\varepsilon$.

In order to clarify the relations among ions in this depth range just before pore close-off, we constructed correlation coefficient matrices, as shown in Table 6. Here, we document the major features of these matrices. Commonly, for the three sites, Na^+, Mg^{2+} and SO_4^{2-} tend to exhibit high positive linear correlation coefficients. Moreover, Cl^- tends to be well correlated with these ions (Na^+, Mg^{2+} and SO_4^{2-}), although in some cases, this is not true at DFS10. Both Ca^{2+} and K^+ are also positively correlated with Na^+, Mg^{2+} or SO_4^{2-}. Commonly, for the three sites, Ca^{2+} and F^- are well correlated with r of 0.45–0.65. Note that SO_4^{2-} is correlated with Na^+ and Mg^{2+} in this depth range (71–92 m) but is not in shallow firn (e.g. the top 4 m at a DF site as reported by Hoshina and others, 2014). This will be confirmed later (Fig. 14).

3.5.2. Depth dependent evolution of the distribution of Na^+ and Cl^- in the $\Delta\varepsilon$–ε_h plot for the DFS10 core

Since Na^+ has a high concentration and the highest positive correlation with ε_h, we focus on the distribution of Na^+ in the $\Delta\varepsilon$–ε_h plot for the DFS10 core, using a dataset of ions produced at RIKEN with depth resolutions of 50–25 mm (measurement ID 4). In addition, we focus on the distribution of Cl^- because Cl^- is highly correlated with Na^+, at least

Table 3. List of samples for detailed investigation of the concentrations of major ions, dielectric permittivity and water isotopes. Five samples of ~0.5 m in length were chosen from a depth range 71–92 m

Core: DF93			Core:DF99			Core: DFS10		
Depth m		Length	Depth m		Length	Depth m		Length
Top	Bottom		Top	Bottom		Top	Bottom	
71.33	71.82	0.49	71.35	71.77	0.42	71.47	71.97	0.50
77.09	77.57	0.48	77.16	77.64	0.48	77.25	77.75	0.50
80.93	81.37	0.44	81.58	82.08	0.50	81.54	82.01	0.48
86.73	87.22	0.49	86.35	86.84	0.49	86.33	86.74	0.41
91.35	91.76	0.41	89.63	90.12	0.49	89.47	89.95	0.48

Measurements with IDs 1, 2 and 5 (Table 1; Fig. 2) were applied to these samples.

within the firn near the ice sheet surface (e.g. Röthlisberger and others, 2003; Hoshina and others, 2014). In Figure 11, the relations between $\Delta\varepsilon$ and the deviatoric ε_h (deviation from the average tendency) are plotted for each ~10 m span for the DFS10 core, as two series, Figures 11a1–h1 and Figures a2 through h2. In these two series of figures, the color of the dots expresses the concentration of Na^+ ions and Cl^- ions with color scales given for these ions. The Na^+ and Cl^- concentrations are clearly related to the evolution of the $\Delta\varepsilon$–ε_h distribution. At the shallowest depth (Figs 11a1 and a2), Na^+ and Cl^- are distributed nearly randomly. However, at greater depths, down to ~30 m (Figs 11b1, b2, c1 and c2), Na^+-rich portions and Cl^--rich portions tend to become denser, being separate from Na^+-poor portions and Cl^--poor portions, respectively. Here, we also observe that denser portions have slightly smaller $\Delta\varepsilon$, indicating that geometrical anisotropy decreased preferentially in the Na^+-rich portions and Cl^--rich portions. Note that we use an expression 'preferential decrease of geometrical anisotropy' in this paper to express decrease of vertically elongated features of ice matrix and pore spaces, detected as decrease of $\Delta\varepsilon$ within some layers, compared with layers surrounding them. We find that, clearly different features appear in the distributions of Na^+ and Cl^- in firn at depths >~30 m. For Na^+ ions, there is no apparent further growth in the color separation between Na^+-rich portions and Na^+-poor portions (see Figs 11d1–h1). In addition, no apparent further preferential decrease in $\Delta\varepsilon$ is observed. These facts indicate that at depths below ~30 m, there is no longer any difference in deformation rate between Na^+-rich portions and Na^+-poor portions. Moreover, preferential decrease of geometrical anisotropy at Na^+-rich portions no longer exists. The distribution of data points on the $\Delta\varepsilon$–ε_h plot, which was formed up to a depth of ~30 m, only rotates in the counterclockwise direction without showing any Na^+ concentration-dependent diffusion along the *x*-axis or *y*-axis. In contrast, for the Cl^- ions the color separation of Cl^--rich portions and Cl^--poor portions smoothes out with increasing depth (Figs 11d2 though h2). At these depths, the distribution of Cl^- again becomes nearly random.

3.5.3. The distribution of Na^+ and Cl^- in the $\Delta\varepsilon$–ε_h plot for the three cores in the depth range just above pore close-off

Figure 11 shows the data over a wide depth range but only for site DFS10. In order to determine whether the same feature is present at sites DF93 and DF99, Figure 12 presents the $\Delta\varepsilon$–ε_h distribution for the cores just above the pore close-off, as listed in Table 3. Na^+ is confirmed to be always localized in the denser side of the distribution, even if the fluctuation of $\Delta\varepsilon$ varies from site to site (see Figs 12a1 - c1). In addition,

Table 4. Statistics for concentrations of major ions, dielectric permittivity and water isotopes for firn from the five depths within the range 71–92 m as listed in Table 3

	F^-	Ca^{2+}	Mg^{2+}	Na^+	Cl^-	NH_4^+	SO_4^{2-}	NO_3^-	K^+	depth	ε_h	$\Delta\varepsilon$	δD	$\delta^{18}O$
Core: DF93														
Mean	0.09	4.84	3.88	29.34	50.68	21.39	102.95	17.99	4.98	81.06	2.733	0.013	−428.77	−55.41
σ	0.07	3.02	1.29	17.16	7.24	8.35	44.14	4.78	3.91		0.074	0.004	6.53	0.84
Max.	0.85	22.58	9.04	177.36	85.32	45.48	286.66	31.08	29.96	91.75	2.859	0.026	−415.09	−53.74
Min.	0.04	1.41	1.13	4.53	37.46	9.69	34.76	11.36	0.91	71.36	2.601	0.005	−442.30	−57.11
Core: DF99														
Mean	0.11	3.10	3.22	23.29	48.85	22.44	96.41	15.74	2.49	81.59	2.716	0.034	−428.92	−55.55
σ	0.29	2.23	1.46	11.62	7.91	8.14	24.43	2.40	1.61		0.071	0.014	7.08	0.90
Max.	2.89	17.02	9.68	73.48	84.09	45.24	177.59	20.71	15.66	90.11	2.829	0.068	−411.92	−53.58
Min.	0.02	0.38	0.18	1.09	31.50	8.40	42.46	11.45	0.49	71.37	2.564	0.011	−445.68	−57.76
Core: DFS10														
Mean	0.07	2.95	3.27	24.15	48.59	35.86	104.23	14.55	1.74	81.20	2.727	0.006	−430.80	−55.76
σ	0.04	1.33	1.26	11.03	12.82	13.96	30.19	3.16	1.18		0.064	0.003	7.71	0.93
Max.	0.33	11.02	7.18	58.72	85.94	70.52	201.74	30.77	10.32	89.94	2.832	0.017	−416.30	−54.06
Min.	0.04	0.72	0.30	1.13	17.08	11.04	34.10	10.60	0.22	71.49	2.598	0.000	−447.86	−57.86

The units for ion concentration and water isotopes are ppb and ‰ respectively, and σ is standard deviation.

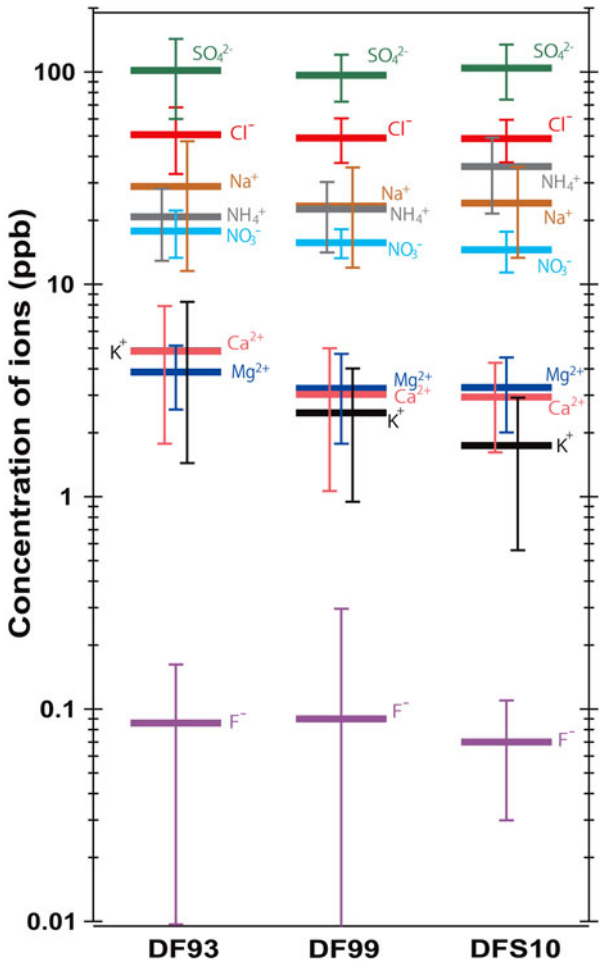

Fig. 9. Concentration of major ions for the selected samples from depths within the range 71–91 m for the three cores as listed in Table 3. The data for this graph are also presented in Table 4. Horizontal markers indicate concentrations of ions. The error bars indicate standard deviations. The concentrations of each ion are approximately the same in the selected samples. There is no evidence that the observed spatial variability of firn densification is a result of different softening/hardening effects by ions.

we confirmed that Cl^- is more smoothed out in the $\Delta\varepsilon$–ε_h distribution (see Figs 12a2–c2 with color scales given for Cl^- concentration). This weaker correlation between Cl^- and the surrogates of densification (ε_h and $\Delta\varepsilon$) also appears in Table 5. Note that at site DF99, Cl^- concentrations are still significantly correlated with ε_h. In addition to these examples of Na^+ and Cl^-, we investigated whether $\Delta^{18}O$ is correlated with the surrogates of densification in Figures 12(a3)–(c3). Smaller values of $\delta^{18}O$ were found to be correlated with larger ε_h and smaller $\Delta\varepsilon$ (Table 5) at site DF99 but not at sites DF93 or DFS10.

3.5.4. Major ions and depth-dependent evolution of correlations

With respect to ions, we tentatively focused only on Na^+ and Cl^-. However, there are many other interesting features of the depth-dependent evolution of correlations between the other major ions, ε_h, $\Delta\varepsilon$ and density. Clearly, we must document these in order to understand processes related to major ions. For example, the depth-dependent variation of Mg^{2+} is always very similar to Na^+ in the shallowest 4 m deep pit at DF sites (Hoshina and others, 2014) until depths close to pore close-off (Fig. 10; Table 5).

An example of ultra-high resolution measurements at 71.46–71.78 m in the DF99 core is presented in Figure 13 (IDs 1, 3, 6 in Fig. 2). The trace of Cl^- is smoother than those for the other ions. In Figures 14a, e, we explore the evolution of the linear correlation coefficients (r) between density (or density surrogate ε_h) and several major ions (Na^+, Cl^-, SO_4^{2-}, Mg^{2+}, Ca^{2+} and NH_4^+) for the DFS10 core and DF99 core, respectively. Note that NH_4^+ data and Ca^{2+} data were available only for the DFS10 core and DF99 core, respectively. As we move from the near surface depths to greater depths, both Na^+ and Cl^- correlations, r, increase with density (or density surrogate ε_h) in both cores, until a depth of ~20–30 m. Then, the trace of Cl^- decreases gradually, whereas the trace of Na^+ continues to increase, again in both cores. Curiously, the depth of separation between traces of Cl^- and Na^+ agree with the depth at which the growth of color separation stopped in Figures 11a1–h1. On the other hand, the linear correlation coefficients (r) between $\Delta\varepsilon$ and ions also have remarkable features. This analysis is available only for the DFS10 core and not for the DF99 core (see Fig. 2; Table 1). As the decrease in geometrical anisotropy proceeds, r should become more negative. In the DFS10 core, on a large scale, negative values of r tend to grow for both Na^+ and Cl^-, together to depths of ~30 m. However, at greater depths, negative correlations gradually disappeared. The data indicate that some mechanism of layered deformation related to Na^+ and Cl^- operates only at limited depths between the near-surface and ~30 m.

The correlation of Mg^{2+} with the surrogates of densification (density, ε_h and/or $\Delta\varepsilon$) are always almost the same as the correlation of Na^+ with these surrogates (Figs 14a, e). The behavior of SO_4^{2-} is also remarkable for both DFS10 and DF99 cores and shows almost no correlation (or weak correlation) with the surrogates of densification (density, ε_h and/or $\Delta\varepsilon$) at the shallowest depth of 20 m (Figs 14a, e). However, at greater depths, SO_4^{2-} starts to exhibit strongly positive correlation with density (or ε_h). Note that r between density (or ε_h) and SO_4^{2-} is always smaller than that between density (or ε_h) and Na^+. Moreover, NH_4^+ ion has weak negative and positive correlations with ε_h and $\Delta\varepsilon$, respectively, in the DFS10 core (Figs 14a). In the DF99 core, Ca^{2+} ion has only weak positive correlation with density (or ε_h) (Fig. 14e).

Finally, we examine the correlations between Na^+ and related anions Cl^- and SO_4^{2-}, in order to clarify the behavior of these ions. In Figures 14c, f, the linear correlation coefficients (r) between Na^+ and Cl^- for the two cores are shown. Here, r values are the highest near the ice sheet surface and decrease with depth. Figures 14d, g show the linear correlation coefficients (r) between Na^+ and SO_4^{2-} for the two cores. Note that r values are smaller near the ice sheet surface and increase with depth.

4. DISCUSSION

4.1. Common conditions at the three sites

4.1.1. Two basic densification phenomena

Firn at the three sites has common features and site-dependent features. We first discuss common features. We list the observed sequence of events within the three firn cores in Table 7. We discuss how this sequence of events can be

Table 5. Linear correlation coefficients between firn chemistry (major ions and water isotopes) and deviatoric ε_h and $\Delta\varepsilon$ for firn from the five depth within the range 71–92 m as listed in Table 3

X and *Y*	Na^+	Mg^{2+}	SO_4^{2-}	Ca^{2+}	K^+	F^-	Cl^-	NH_4^+	NO_3^-	δD	$\delta^{18}O$
Core: DF93											
Logarithmic values vs deviatoric ε_h	**0.43**	**0.43**	**0.41**	−0.08	−0.03	0.04	0.16	−0.09	−0.06		
Linear values vs deviatoric ε_h	**0.26**	**0.39**	**0.38**	−0.07	−0.04	0.03	0.14	−0.02	−0.02	**−0.25**	**−0.21**
Logarithmic values vs $\Delta\varepsilon$	−0.16	**−0.20**	**−0.22**	0.15	−0.04	−0.03	−0.09	**0.17**	**0.25**		
Linear values vs $\Delta\varepsilon$	−0.09	**−0.24**	**−0.21**	0.15	−0.09	0.02	−0.08	0.10	**0.21**	**0.21**	**0.18**
Core: DF99											
Logarithmic values vs deviatoric ε_h	**0.70**	**0.71**	**0.47**	**0.42**	**0.32**	−0.10	**0.50**	**−0.37**	**−0.16**		
Linear values vs deviatoric ε_h	**0.60**	**0.63**	**0.46**	**0.18**	0.14	−0.09	**0.48**	**−0.33**	−0.15	**−0.53**	**−0.50**
Logarithmic values vs $\Delta\varepsilon$	0.13	0.10	0.05	**0.41**	**0.46**	**0.30**	0.15	**0.52**	**−0.22**		
Linear values vs $\Delta\varepsilon$	0.10	0.07	0.06	**0.40**	**0.46**	**0.23**	0.14	**0.56**	**−0.24**	**0.23**	**0.28**
Core: DFS10											
Logarithmic values vs deviatoric ε_h	**0.51**	**0.53**	**0.41**	**0.35**	**0.44**	**0.25**	0.12	−0.06	0.12		
Linear values vs deviatoric ε_h	**0.51**	**0.53**	**0.38**	**0.27**	**0.33**	**0.18**	**0.17**	−0.05	0.11	**−0.17**	−0.16
Logarithmic values vs $\Delta\varepsilon$	**0.23**	**0.23**	**0.16**	**0.20**	**0.22**	0.13	−0.05	0.09	0.05		
Linear values vs $\Delta\varepsilon$	**0.23**	**0.24**	0.14	**0.19**	**0.18**	**0.18**	−0.01	0.08	0.09	−0.10	−0.12

Bold values indicate significant correlations ($p < 0.001$).

explained. We hypothesize that there are two basic phenomena. One of which is the evolution of the counterclockwise 'rotation' of the data distributions, as observed in Figure 6. This phenomenon is hypothesized to be caused by textural effects, as discussed in detail previously (Fujita and others, 2009). The other phenomenon is, as we have observed in Section 3.5, preferential deformation, which temporally occurs in the shallowest ~30 m, of Na^+-rich layers. However, this phenomena are probably more complex: we hypothesize that Cl^- dissociated from sea salts is one of the active agents of the enhanced deformation. Softening effects of ice is explained by the presence of Cl^- in the lattice of ice crystal lattice. Here, we explain how we identify and understand these two basic phenomena. To help readers to better understand the discussion, we have provided in Table A8, a summary list of earlier discussions of 'facts, explanations and related notes for the densification of polar firn'.

4.1.2. *Initial formation of layering*

In order to clarify all phenomena within the firn, the initial formation of layering should be clarified. Near DF, Antarctica, summer layers have been reported as hard and dense while

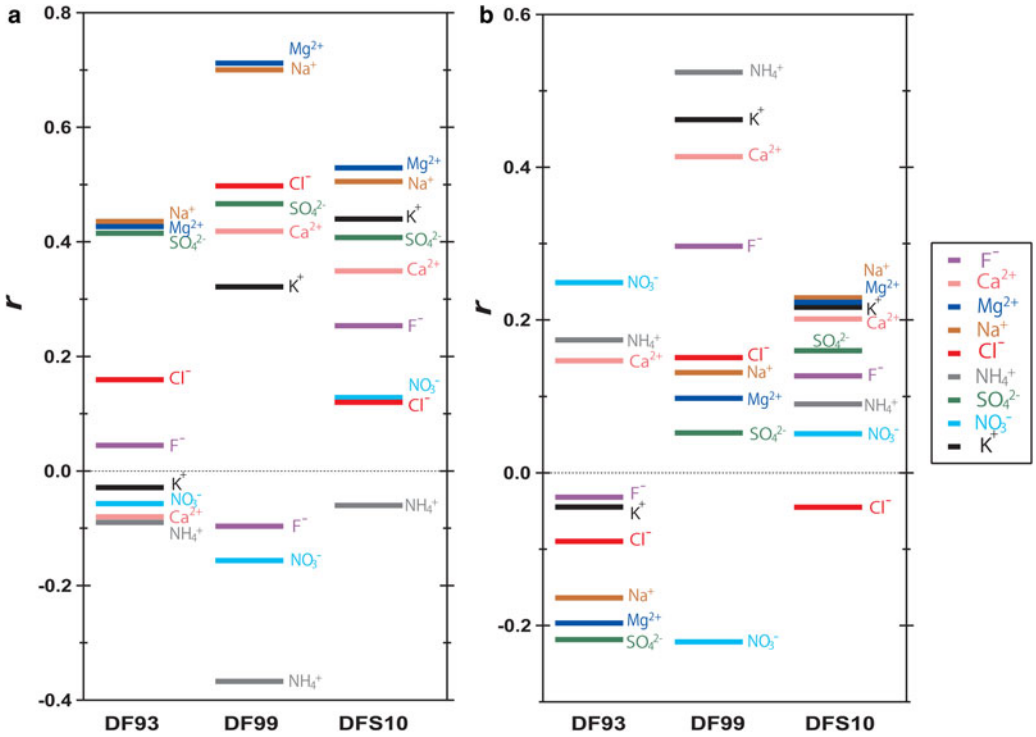

Fig. 10. Linear correlation coefficients (r) between the indicator of densifications (ε_h and $\Delta\varepsilon$) and the concentration of major ions for the selected samples from depths within the range 71 to 91 m for the three cores as listed in Table 3. Panels (a) and (b) show r for ε_h and $\Delta\varepsilon$, respectively. When $|r| > \sim 0.3$, r is statistically significant. In (a), ε_h has strong positive correlations with Na^+, Mg^{2+} and SO_4^{2-} ions. ε_h tends to have weak positive correlations with Cl^- ions. ε_h tends to have weak negative correlation with NH_4^+ ions. There is no clear tendency of r between ε_h and F^-. In (b), $\Delta\varepsilon$ tends to have weak positive correlations with NH_4^+. For most other ions, including Cl^- and F^-, $\Delta\varepsilon$ appears to have only random (or no) correlations.

Table 6. Correlation coefficient matrix for ion species for firn from the five depths within the range 71–92 m within the three firn cores listed in Table 3

	Mg^{2+}	Na^{+}	SO_4^{2-}	K^{+}	Ca^{2+}	NO_3^{-}	F^{-}	Cl^{-}	NH_4^{+}
Core: DF93									
Mg^{2+}	1								
Na^{+}	**0.73**	1							
SO_4^{2-}	**0.45**	**0.24**	1						
K^{+}	**0.51**	**0.68**	0.06	1					
Ca^{2+}	**0.40**	**0.65**	0.15	**0.65**	1				
NO_3^{-}	**−0.23**	0.11	**−0.36**	0.10	0.12	1			
F^{-}	**0.31**	**0.83**	0.03	**0.65**	**0.64**	**0.27**	1		
Cl^{-}	**0.66**	**0.68**	0.02	**0.62**	**0.44**	−0.04	**0.49**	1	
NH_4^{+}	−0.11	**0.19**	0.02	**0.22**	**0.35**	**0.72**	**0.32**	−0.15	1
Core: DF99									
Mg^{2+}	1								
Na^{+}	**0.99**	1							
SO_4^{2-}	**0.67**	**0.67**	1						
K^{+}	**0.35**	**0.41**	**0.26**	1					
Ca^{2+}	**0.34**	**0.38**	**0.17**	**0.87**	1				
NO_3^{-}	**−0.20**	**−0.24**	**−0.26**	**−0.40**	**-0.29**	1			
F^{-}	−0.05	0.01	−0.02	**0.45**	**0.59**	−0.14	1		
Cl^{-}	**0.76**	**0.78**	**0.18**	**0.49**	**0.49**	**−0.29**	0.13	1	
NH_4^{+}	**−0.22**	**−0.17**	0.14	**0.45**	**0.28**	**−0.22**	**0.23**	**−0.16**	1
Core: DFS10									
Mg^{2+}	1								
Na^{+}	**0.97**	1							
SO_4^{2-}	**0.58**	**0.52**	1						
K^{+}	**0.51**	**0.65**	**0.22**	1					
Ca^{2+}	**0.37**	**0.34**	**0.22**	**0.34**	1				
NO_3^{-}	**0.33**	**0.31**	−0.10	0.13	−0.08	1			
F^{-}	**0.30**	**0.24**	0.13	0.14	**0.57**	**0.49**	1		
Cl^{-}	0.15	**0.22**	0.09	**0.34**	0.12	**−0.62**	**−0.35**	1	
NH_4^{+}	**−0.20**	**−0.23**	−0.06	**−0.28**	**0.24**	**−0.29**	−0.03	0.10	1

Bold values indicate significant correlations ($p < 0.001$).

the winter section is softer, coarser-grained and more homogeneous (Koerner, 1971; Shiraiwa and others, 1996). For convenience, Fujita and others (2009) referred to these two types of firn as initially high density firn (IHDF) and initially low density firn (ILDF). These terms are used to roughly specify the initial state of the layers at the near-surface, even after they are modified at greater depths by metamorphism. Based on a thorough investigation of the effect of summer warmth and solar radiation through stratigraphic comparisons in early December and late January, Koerner (1971) found that, the IHDF is formed when drifting of surface hoar formed in wind speed is $>4\ m\ s^{-1}$. He found that ice bridges formed between grains. More recently, Fujita and others (2008) investigated temporal and spatial changes in the density of surface snow to a thickness of 0.2 m in the DF region, during the summer, December 2007 to January 2008. They found that new soft snow tended to change into compacted harder snow during the short 1-month period investigation. In addition, more densification occurred at shallower depths.

Hoshina and others (2014) investigated layers in water stable isotopes and major ions in firn using a 4 m deep pit at DF. In their study, they found there were variations of Na^{+}, Cl^{-} and is $\delta^{18}O$ with multiyear cycles, and that the cycles exhibited no significant correlations with density fluctuations. Therefore, the formation of the density layering is a phenomenon that is not closely related to the formation of the layering of Na^{+}, Cl^{-} or $\delta^{18}O$. We partly confirm this situation based on the data shown in Figures 11a1, a2 and 14a, b, e. The concentration of Na^{+} has no or weak correlation with the distributions of ε_h (and thus density) or $\Delta\varepsilon$.

In summary, we hypothesize that IHDF forms at the surface during the summer, presumably related to the redistribution of ice particles by wind and deposition under summer insolation. In addition, density layering has no significant correlations with multiyear cycles of Na^{+} (and other major ions) or $\delta^{18}O$. At near surface depths in the ice sheet, the fluctuations of the density surrogate (σ_h) have maximum amplitude (Fig. 8). Moreover, $\Delta\varepsilon$ has maximum values (Figs 5, 6). The correlations between ε_h and $\Delta\varepsilon$ also have maximum values (Fig. 7), which means that denser firn has stronger geometrical anisotropy in the microstructure. This feature is robust in both the DF region (present study; Fujita and others, 2009) and in the Greenland NEEM Camp (Fujita and others, 2014).

4.1.3. *Initial stage of densification: 0 m to ~40 m*

The initial stage of densification is characterized by a number of figures in the present study. Firn becomes denser only gradually without any visible inflections (Figs 3–8, 11). As suggested previously, based on observations (Fujita and others, 2009), ILDF tends to deform more preferentially than IHDF, resulting in counterclockwise rotation of the data distribution in the ε_h–$\Delta\varepsilon$ plot (Figs 6, 7, 11). Since there is clear continuity in the counterclockwise rotation of the data distribution, preferential deformation of ILDF, compared with IHDF, occurs throughout the densification processes from the near surface depths to depth of the pore close-off. On the other hand, as observed and described in

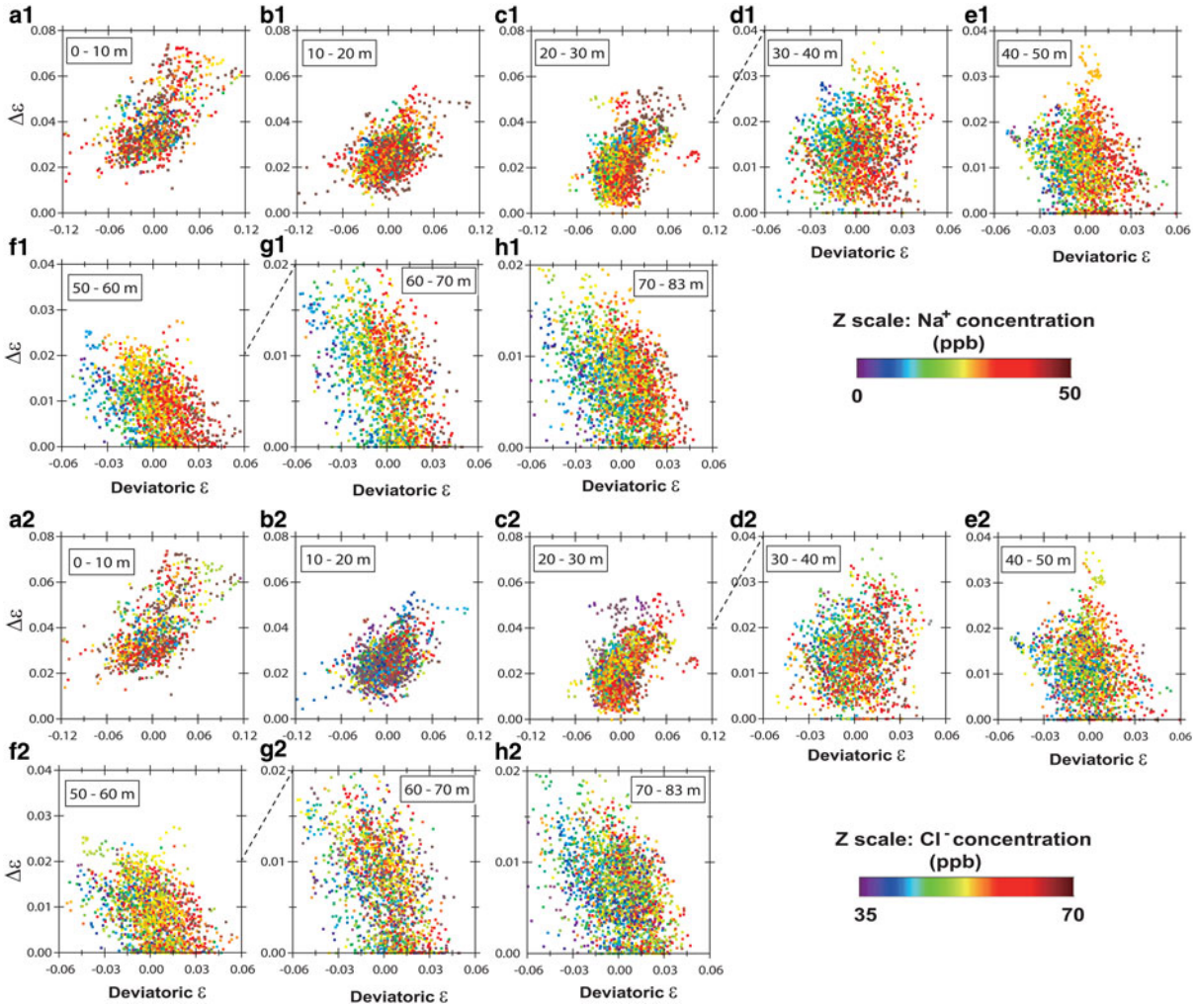

Fig. 11. For the DFS10 core, data points of $\Delta\varepsilon$ vs deviatoric ε_h (deviation from the average tendency) are plotted for each ~10-m-deep span. Each dot represents a measurement of $\Delta\varepsilon$ and ε_h. For panels (a1)–(h1), the color of each dot indicates the concentration of Na^+ ions in the same portion of the sample. In panels (a2)–(h2), the data distribution of the $\Delta\varepsilon$–ε_h plots is the same as those in panels (a1)–(h1). However, in these figures, dot colors indicate the concentration of Cl^- ions in the sample. Panels (a1)–(h1) and (a2)–(h2) show the contrasting distributions of the Na^+ and Cl^- ions. For concentration of Na^+ ions and Cl^- ions, scale bars are given on the right-hand side. The data for each of the ions with a depth resolution of 40 mm are linearly interpolated to depth steps of 5 mm for $\Delta\varepsilon$ and ε_h. Note that the scales of the vertical axis are expanded twofold at (d) and again at (g). In addition, the scales of the horizontal axis are expanded twofold once at (d). Generally, preferential densification occurs in samples with smaller $\Delta\varepsilon$ values. This tendency drives the transition from positive (panels (a)–(c)) to negative correlations (panels (d)–(h)). In addition, Na^+- and Cl^--rich portions rapidly become denser from the surface to a depth of ~30 m. However, below 30 m, no further separation between Na^+-rich portions and Na^+-poor portions appears to occur. In these $\Delta\varepsilon$–ε_h plots, Cl^- ions are more homogeneously distributed in firn than Na^+ ions.

Section 3.5, Na^+-rich layers and Cl^--rich layers deform preferentially only during the initial stage.

Next, we discuss a mechanism that modified the deformation rate of the Na^+-rich layers and Cl^--rich layers only during the initial stage. We hypothesize that the most plausible cause of this modification is the deformation enhancement associated with the presence of Cl^- ions. Note that, Hörhold and others (2012) speculated that the impurity content in terms of particulate dust is localized at the grain boundaries and triple junctions, and that it might increase the thickness of the quasi-liquid layer coating of individual grains, resulting in softening of firn. However, Fujita and others (2014; Section 4.3.3) argued that no reliable evidence suggests that dust particles significantly soften ice; cations such as Na^+, Ca^{2+} and Mg^{2+} are unlikely to enhance deformation. The Cl^- ion is known to modulate dislocation movement in the ice crystal lattice if it is substituted for the location of H_2O atoms in ice (Jones, 1967; Jones and Glen, 1969; Nakamura and Jones, 1970). Thibert and Domine (1997) found that solid ice is slightly soluble in the presence of HCl and that its diffusivity through a single crystal is slightly smaller than the self-diffusion of water molecules. Ion species can be transported by molecular diffusion in firn and ice (Johnsen and others, 2000; Livingston and George, 2002; Barnes and others, 2003, Iizuka and others, 2006). Barnes and others (2003) reported that direct diffusion through solid ice is too slow to explain the observed diffusion in firn and ice at the Dome C ice core. However, liquid acids H_2SO_4, HCl, HNO_3 and so on, diffuse especially rapidly (e.g. Barnes and others, 2003). The circumstantial evidence for the deformation enhancement effects associated with the Cl^- ion is that apparent preferential densification of the Na^+-rich layers ceases when strong correlation between Na^+ and SO_4^{2-} occurs (Figs 11, 14). This means that sea salt sulfates (e.g. Na_2SO_4 and $MgSO_4$) form when sea salts (e.g. NaCl and $MgCl_2$) and H_2SO_4 meet in firn, releasing free HCl in

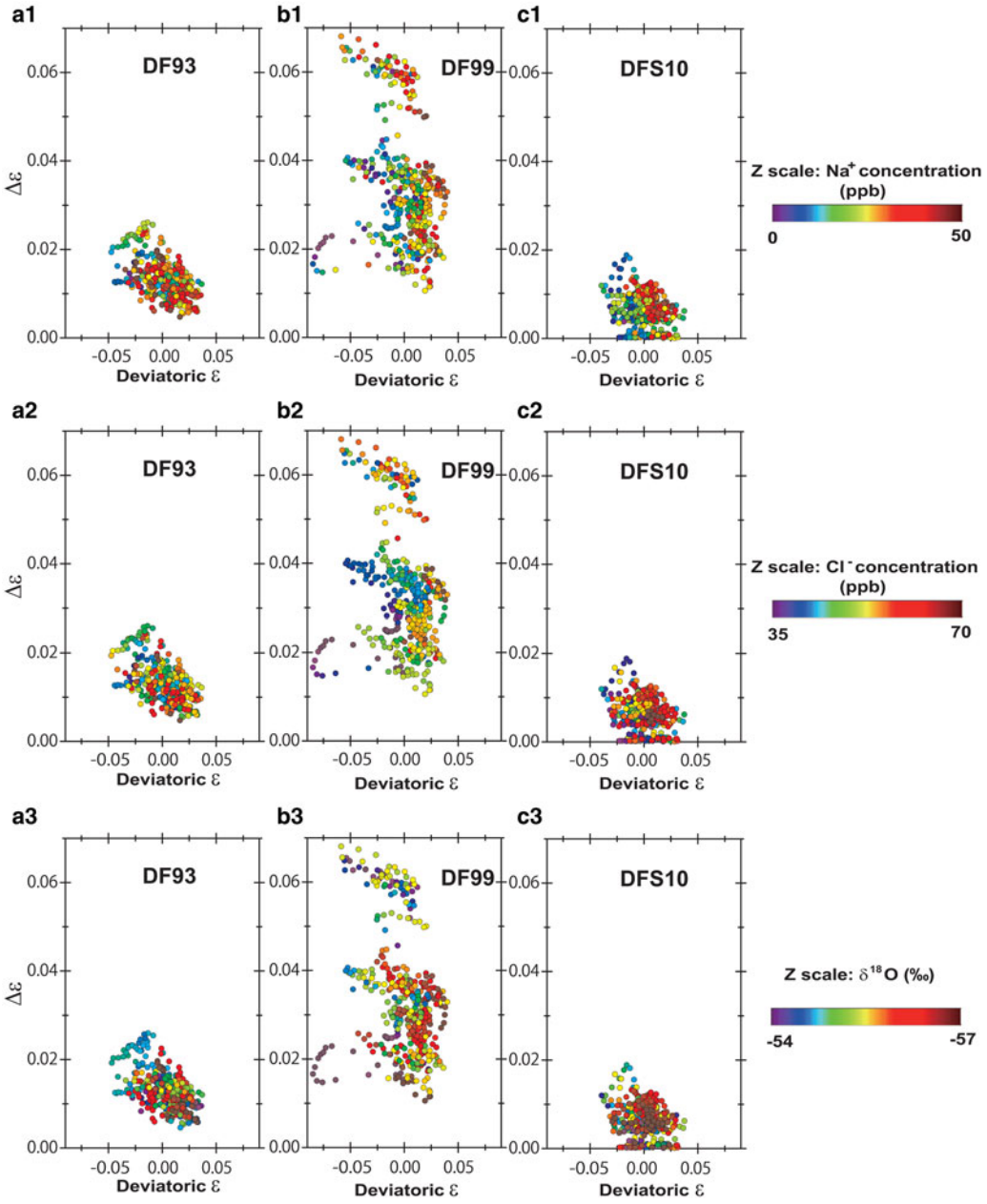

Fig. 12. As in Figure 11, the data points of $\Delta\varepsilon$ vs deviatoric ε_h are plotted for the selected samples from depths within the range 71–91 m for the three cores, as listed in Table 3. The three rows of plots present information of Na^+ concentration (top), Cl^- concentration (middle) and oxygen isotope ratio (bottom). Color scales are also given on the right in each row. Even if $\Delta\varepsilon$ values vary from one site to another, preferential densification tends to occur in samples with smaller $\Delta\varepsilon$ values. Na^+-rich portions and Na^+-poor portions are clearly separated in terms of deviatoric ε_h, but not in terms of $\Delta\varepsilon$ ((a1)–(c1)). Similarly, Cl^--rich portions and Cl^--poor portions are also separated in terms of deviatoric ε_h ((a2)–(c2)). In the bottom ((a3)–(c3)), firn with smaller values of $\Delta^{18}O$ have larger values of deviatoric ε_h and smaller values of $\Delta\varepsilon$ at site DF99. However, this tendency is unclear at the other two sites (DF93 and DFS10) (Table 5).

firn (e.g. Iizuka and others, 2004a, 2006, 2012). It is reasonable that no preferential deformation (by this impurity mechanism only) occurs when Cl^- is smoothed out by diffusion in various mechanisms, in solid, liquid, or vapor phase (e.g. Barnes and others, 2003). In addition, Cl^- always diffuses from its original site of sea salts. This explains why layered densification seemingly proceeds at locations of higher Na^+ (and Mg^{2+}) concentration. The original site of sea salts has high probability for temporal residence of Cl^- in the ice lattice. Although these cations are not a direct cause of the preferential deformation, preferential densification at locations of these cations is explained assuming that these cations are left as 'markers' of temporarily enhanced deformation.

4.1.4. *Sequence of evolution of densification: 40–80 m*

Near zero linear correlation coefficients between ε_h and $\Delta\varepsilon$ were reached at 30–40 m (Fig. 7). In addition, the local convergence of density is reached at ~40 m (Fig. 8). These phenomena are clearly caused by the counterclockwise rotation of the data distribution in the ε_h–$\Delta\varepsilon$ plot (Figs 6, 7, 11). We observed maximum correlation between density ρ and Na^+ concentration at a greater depth of 50–60 m (see Figs 14a and e). Although it may appear as if Na^+ were still causing preferential deformation, a closer look at Figure 11 reveals that this is not the case. The apparent separation between the Na^+-rich portions and the Na^+-poor portions occurs dominantly only during the initial

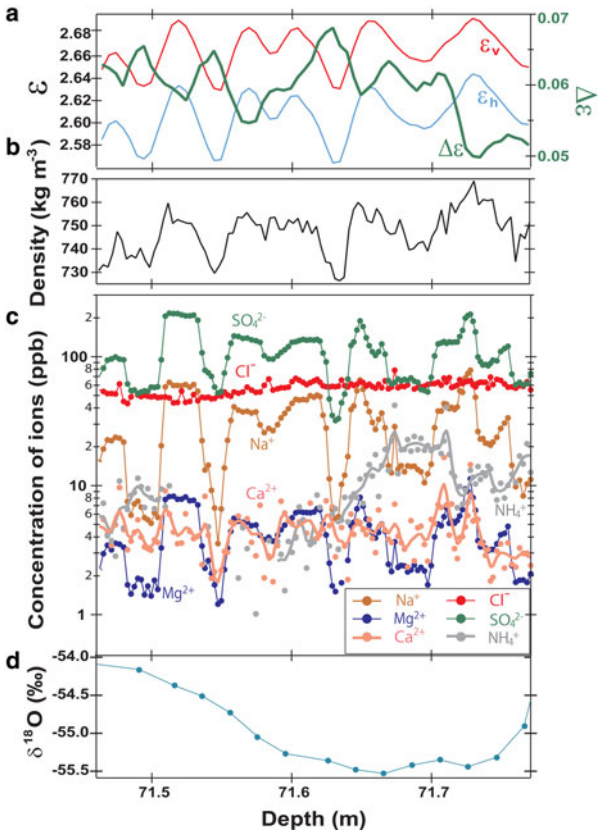

Fig. 13. An example of tensorial components of dielectric permittivity (ε_v and ε_h), dielectric anisotropy ($\Delta\varepsilon$), density (ρ), concentrations of several major ions and values of $\delta^{18}O$ in the DF99 firn core. This example is for a 0.3 m core at a depth range in which σ_h is well developed as local maxima in Figure 8. The abscissa shows the depth. The density ρ was measured at a resolution of 3.3 mm using a gamma-ray transmission method at NIPR. The concentration of ions was measured at a resolution of 2 mm at ILTS. $\delta^{18}O$ was measured at NIPR. The physical features (such as ε_v, ε_h, $\Delta\varepsilon$ and ρ) are well correlated with SO_4^{2-}, Na^+, Ca^{2+} and Mg^{2+}. The Cl^- ion is smoothed compared with the other ions, such as Na^+. $\delta^{18}O$ has only large-scale variations.

stage (0–30 m). When this initial separation occurs, Na^+-rich layers (dots in the figure) tend to localize at the right-bottom side because of densification (with increasing ε_h) and slight decrease of geometrical anisotropy (with slightly decreasing $\Delta\varepsilon$) (Fig. 11c1). This localization in the ε_h–$\Delta\varepsilon$ plot is conveyed and rotated by the counterclockwise rotation of the data distribution, thereby showing the maximum correlation between ε_h and Na^+ concentration only at 50–60 m (Figs 11e1, e2 and 14a, e). The initial localization at the bottom right-hand side moves to the right-hand side as a result of the rotation. Therefore, the maximum correlation is explained only (or mostly) by the rotation, rather than by further growth of the layered densification caused by impurities.

At these greater depths, we find the local maximum of density fluctuations (σ_h) at a depth range of 60–80 m (Fig. 8). At the same depth range, the correlation between ε_h and $\Delta\varepsilon$ is minimal (Fig. 7). These phenomena are also directly related to the counterclockwise rotation of the data distribution in the ε_h–$\Delta\varepsilon$ plot. When the ILDF deforms preferentially, because of the deformation of the pore geometry, $\Delta\varepsilon$ becomes smaller, resulting in a more negative correlation between ε_h and $\Delta\varepsilon$. However, ~78 m is the starting depth of bubble close-off at site DF93 (Fujita and others, 2009). Near this depth, the firn density approaches the pore-closing density of 830 kg m^{-3}; the firn has less pore space remaining for further deformation. Such conditions are reached preferentially in more-deformed layers. At the same time, the density of the less-deformed layers starts to catch up with that of the more-deformed layers. Therefore, σ_h starts to decrease. Moreover, the correlation between ε_h and $\Delta\varepsilon$ starts to approach zero.

4.2. Basic role of ions that can modulate dislocation movement in the ice crystal lattice

In this section, we consider questions as to how ions such as F^-, Cl^- and NH_4^+ can affect densification. As discussed above, a series of observational facts are explained if we hypothesize that Cl^--rich layers deform preferentially. When Cl^- is smoothed out spatially, instead of developing layered and heterogeneous deformation, Cl^- should enhance the deformation of firn and ice homogeneously. Note that the Cl^- concentration is as high as 50 ppb (Table 4), which can modulate the deformation rate of ice by several percent if laboratory data from earlier studies are scaled linearly (Jones, 1967; Jones and Glen, 1969; Nakamura and Jones, 1970). In the case of NH_4^+, as described in Section 3.5, the presence of NH_4^+ appears to have caused hardening, similar to the small hardening of NH_4^+-doped single-crystal ice (Jones and Glen, 1969). In addition, the concentration of NH_4^+ is within 21–36 ppb (Table 4), which can modulate the deformation rate of ice by several percent. The F^- ion has the strongest correlation with densification in the case of the Greenland NEEM core, with mean and maximum concentrations of 0.22 and 2.38 ppb (Fujita and others, 2014). In the present study, the mean and maximum concentration of F^- are in the range 0.07–0.11 ppb and 0.03–2.89 (Table 4). Although at the DF sites concentration of F^- is smaller than that in the case of NEEM, we still expect that F^- can modulate the deformation rate of ice by several percent. It is possible that F^- may be smoothed out by diffusion, obscuring the markers of temporarily localized densification under the very low annual accumulation rate at these sites.

In summary, we hypothesize that F^-, Cl^-, and NH_4^+ ions can actually enhance/suppress deformation in firn/ice in Antarctic DF sites, as suggested by the example of the NEEM camp. When these ions are present in a layered condition, they can cause the layered deformation either by enhancing or suppressing. Once these ions are smoothed out by diffusion, it is natural that layered deformation – caused by these impurities only – ceases. However, even after the smoothing out, these ions should work to enhance/suppress ice deformation homogeneously at DF sites. When the annual accumulation rate is higher, as in the Greenland NEEM case (~ 8 times that of DF), layered deformation can continue persistently because diffusion does not easily smooth out annual layers of these ions (see such examples in Figs. 9, 10 in Fujita and others, 2014). The effect of these ions acts at dislocations in the crystal lattice, basically independently from more macroscopic textural effects, assumed to be related to ice–ice bonding, crystal orientation fabrics and the geometry of pore spaces and ice. Even if layered deformation proceeds due to these ions, basic counterclockwise rotation can proceed independently at DF sites (Fig. 11).

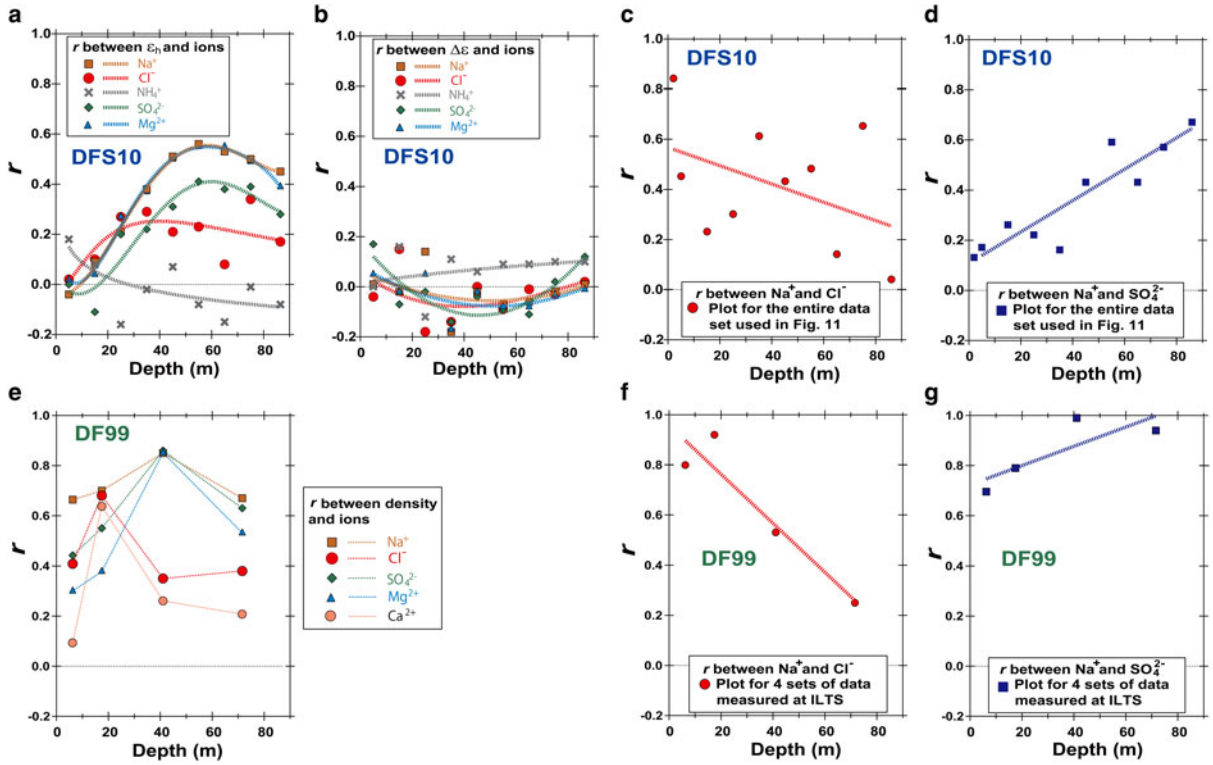

Fig. 14. For the DFS10 and the DF99 cores, linear correlation coefficients (r) between various firn properties are given. (a)–(d) DFS10 core. (a) r between indicators of densification (ε_h) and concentration of key ions (Na^+, Cl^-, SO_4^{2-}, Mg^{2+} and NH_4^+). (b) r between indicators of decrease of geometrical anisotropy $\Delta\varepsilon$ and the concentrations of key ions. (c) r between concentrations of Na^+ and Cl^-. (d) r between concentrations of Na^+ and SO_4^{2-}. (e)–(g) DF99 core. (e) r between density and concentration of key ions (Na^+, Cl^-, SO_4^{2-}, Mg^{2+} and Ca^{2+}). (f) r between concentrations of Na^+ and Cl^-. (g) r between concentrations of Na^+ and SO_4^{2-}.

We note here, that each layer keeps memory of its initial state of the textural features even if they are partially modified by the effect of impurity-based softening/hardening. Memory of ice–ice bonding should still be preserved unless such bonding is disconnected by dislocation creep, which seems unlikely. The effect of impurities is that, vertically elongated ice matrix and pore spaces may shrink to some extent. However, the implication of Figure 11c1 is that even if such densification occurs, it causes only a slight decrease in $\Delta\varepsilon$. In Figure 11c1, separation of color in the x-direction (density direction) is clear but color separation in the y-direction (anisotropy direction) is weak. This feature is also visible as weak correlations between impurity and $\Delta\varepsilon$ in Figure 14b. Based on this preservation of $\Delta\varepsilon$, we hypothesize that the textural effects from the initial state keep effective throughout the whole firn column.

4.3. Implication for the local insolation modulation of gas transport conditions during bubble close-off

Fujita and others (2009) hypothesized that the strength of the textual effects determines the duration for firn-to-ice transition and so determines the degree of lower O_2/N_2 ratio and smaller TAC. More recently, based on the empirical correlations between Ca^{2+} concentrations and densification enhancement, Hörhold and others (2012) suggested that seasonal density-layering loses its initial stratigraphic information in the top 10–15 m of the firn column, and therefore a direct line of influence of the local radiation balance on the surface snow density cannot be the ultimate reason for the observed O_2/N_2 fractionation at close-off depth. In the present study, based on the data and the explanations, we hypothesize as follows: (1) density-layering does not lose its initial textural information in the shallow portion (10–15 m in the Hörhold and others (2012) cases and 0–30 m at DF) of the firn column, though some ions provide additional features to the initial density-layering. The preserved textural features robustly cause counterclockwise rotation of the data points in the $\Delta\varepsilon$–ε_h space, which is independent of the impurity effects. (2) Therefore, a direct line of influence of the local radiation balance on the surface snow density is the basic reason for the observed O_2/N_2 fractionation at close-off depth.

In addition, we note that horizontal continuity of the firn layers should be limited to the order of meters or less – the scale of irregular topographic reliefs of the snow surface – (e.g. Kameda and others, 2008; Koerner, 1971). Fujita and others (2009; Section 4.3) discussed effects of the irregular shape of the snow surface on air bubble formation and permeability processes within firn. They hypothesized that both ILDF and IHDF form a 3-D network: 3-D paths of air diffusion are preserved down to depths very close to pore close-off depth (~104 m at DF93 site).

4.4. Spatial variability in firn properties at the three sites

The three sites exhibit the spatial variability of firn properties. Remarkable spatial variability occurs even within ~100 m of sites DF93 and DF99 and within ~10 km, the distance from site DFS10 to site DF93/site DF99. The initial properties of snow are basically determined by the surface conditions of

Table 7. Sequence of events within the firn cores near DF

Depth range	Event	Reference figure(s)
Near surface depths[a]	Maximum amplitude of density (and thus ε_h) fluctuations, to decrease	8
	Maximum values of $\Delta\varepsilon$, to decrease	5
	Maximum correlation between ε_h and $\Delta\varepsilon$, to decrease	7
	No correlation between density (and thus ε_h) and Na^+, to increase	13
	Preferential deformation for the Na^+-rich layers and thus Cl^--rich layers starts	11, 14a, e
	Maximum correlations between Na^+ and Cl^-, to decrease	14c, f
	Minimum of correlations between Na^+ and SO_4^{2-}, to increase	14d, g
30–40 m	Zero correlation between ε_h and $\Delta\varepsilon$ is reached	7
	Local convergence of density (and thus ε_h) fluctuations is reached	8
	Preferential deformation for the Na^+-rich layers and thus Cl^--rich layers ceases	11
~55 m	Maximum correlation between density (and thus ε_h) and Na^+ is reached, to decrease	14a, e
60–80 m	Local maximum of density (and thus ε_h) fluctuations is reached, to decrease	7
	Minimum negative correlation between ε_h and $\Delta\varepsilon$ is reached, to be closer to zero	8
80–104 m	Formation of air bubbles in ice and pore close-off at ~104 m	4 and Figure 9 in Fujita and others (2009)
~120 m	Zero correlation between ε_h and $\Delta\varepsilon$ is reached	7

[a]Maximum and minimum values start to decrease and increase, respectively, with increasing depths.

the ice sheet, such as the accumulation rate, temperature, temperature gradient and wind conditions (references given in the introduction). The annual accumulation rates at sites DFS10 and DF99 are 96.7% (±0.2%) and 98.9% (±0.2%), respectively, of that of DF93 (Table 2). The surface temperature is assumed to be very similar at the three sites because these sites are very close to each other. The location relative to the ice divide (Fig. 1) may cause differences in wind conditions at the three sites. We assume that the windward side of sites DF93 and DF99 is exposed to winds of different strength compared with the leeward side at site DFS10. We also assume that the windward side of sites DF93 and DF99 is exposed to moister wind than the leeward side at site DFS10 (Fujita and others, 2011). In addition, there are faint differences in the ice sheet surface slope and curvature caused by bedrock topography (note the surface topography undulations shown in Figure 1b and Fujita and others, 2011),

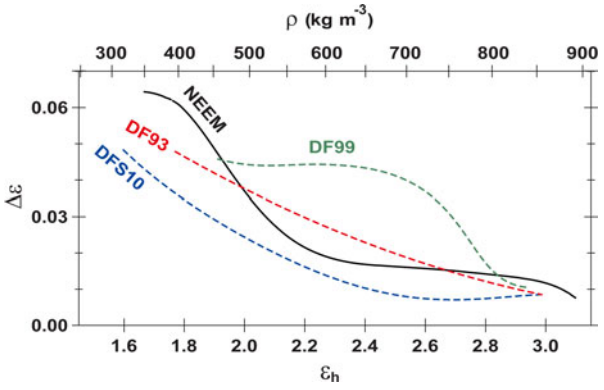

Fig. 15. Plots of $\Delta\varepsilon$ vs ε_h for the three firn cores near DF in Figure 6 and data of the North Greenland Eemian Ice Drilling (NEEM) core. The top axis shows the density of firn equivalent to ε_h of the bottom axis. At NEEM, the bend of the curve in the $\Delta\varepsilon$–ε_h plot is clear at a density of ~600 kg m^{-3} In contrast, no such strong bend is observed near DF.

which is directly related to surface mass balance (SMB). Therefore, we speculate that differences in (1) SMB, (2) wind conditions and (3) ice sheet surface slope and curvature and (4) the location in reference to ice divide determined the variability in firn properties. More detailed discussions are beyond the scope of this paper.

4.5. Comparison with the Greenland NEEM core

In Figure 15, we present $\Delta\varepsilon$–ε_h plots for the three firn cores near DF as well as those at the NEEM camp (Fujita and others, 2014). Conditions such as temperature, accumulation rate, wind, strain rate and amount and seasonality of ions are different for DF and the NEEM camp. The SMB at NEEM is ~ 8 times larger than that at DF. Remarkably, $\Delta\varepsilon$ decreases with density ρ, and the depth z is more gradual and smoother compared with that at NEEM camp. At NEEM, $\Delta\varepsilon$ decreases rapidly from the surface up to a density of ~600 kg m^{-3}. After that, $\Delta\varepsilon$ decreases with a much less steeper slope. This means that, unlike at NEEM, the anisotropy of ice and pore spaces is larger and is preserved for a much longer period at DF, without any discontinuous features. Fujita and others (2014) suggested that the layered deformation at NEEM is partly due to the textural effects initially formed by the seasonal variation of metamorphism and partly due to softening/hardening effects of ions such as F^-, Cl^- and NH_4^+. It is reasonable that textural effects imprinted by insolation at DF are much stronger than at NEEM, because the residence time of firn near the surface is ~ 8 times longer. The inflected trace at NEEM in Figure 15 implies that the deformation of firn occurs easily due to weaker textural strength. In the present study, we investigated the softening/hardening effects of Cl^- and NH_4^+. For the NEEM case, the effects of F^- and Cl^- were reported in a previous study. Overall, we suggest that all the ions, F^-, Cl^- and NH_4^+, that were identified to modulate dislocation movement in ice (Jones, 1967; Jones and Glen, 1969; Nakamura and Jones, 1970) play important roles in creep deformation of polar firn and ice.

5. CONCLUDING REMARKS

The evolution of ε_h and $\Delta\varepsilon$ were investigated based on information concerning impurity ions and water stable isotopes for the three cores near Dome Fuji. We suggest answers for the four questions posed in Section 1 as follows:

(1) We observed significant correlations between ions such as Cl^- and NH_4^+ and layered enhancement of deformation, like the Greenland NEEM case. Observed phenomena are explained if we assume that ions such as Cl^-, F^- and NH_4^+ are the active agent in the layered deformation.
(2) We suggest that the softening/hardening effects due to these ions are independent of the textural effects. Actual layered densification is a complex phenomenon that occurs as a result of these two independent effects. In previous studies, Freitag and others (2013) and Hörhold and others (2012) empirically discovered a strong correlation between deformation and Ca^{2+}. We infer that either F^- or Cl^-, or both F^- and Cl^- were correlated with Ca^{2+}, because Cl^- was strongly correlated with Na^+ near the ice sheet surface. F^- and Ca^{2+} are closely correlated both at the DF region (Table 6) and at Greenland NEEM (Fujita and others, 2014), implying that softening effects by F^- are instead recognized as high correlation between density and Ca^{2+}. We speculate that dissociation of F^- ions from fluorite (CaF_2) dusts by reaction with H_2SO_4 may be related. A full understanding of the firn densification problems requires knowledge of both textural effects and softening/hardening effects by ions. During glacial periods, there is generally a higher concentration of impurity ions and dusts. During such periods, the softening/hardening effects by ions will be more significant. Even if these ions are smoothed out in firn, they will soften or harden ice in a smooth (homogeneous) manner. The effects should be considered for modeling the flow of the ice sheet.
(3) Spatial variability appears in nature and evolution of firn because both depositional conditions and subglacial conditions are highly variable spatially, even around the DF summit (e.g. Fujita and others, 2011, 2012). Surface conditions of the ice sheet are often influenced by subglacial conditions because of the influence on curvature of the ice sheet surface. The location of the site relative to the ice divide or dome summit, such as the windward or the leeward side, is also a very important factor.
(4) Metamorphism and initial layering of snow is dependent on various surface conditions, such as the accumulation rate, temperature, temperature gradient, mechanical forcing by wind, insolation and probably the average humidity of ambient air. We hypothesize that the mechanical strength due to the textures of the layers is determined by these initial conditions. Generally, preferential deformation of the ILDF, as compared with IHDF, occurs throughout the densification processes from the near surface depths to the pore close-off depth. The counterclockwise rotation of the data distribution in the ε_h–$\Delta\varepsilon$ plot (Figs 6, 7, 11) represents the sequence of the textural effects.

Based on conditions (3) and (4), features of firn from the three sites are markedly different in terms of the strength of the geometrical anisotropy, the mean rate of densification and density fluctuation.

In the future, we intend to:

(1) Quantify in detail, the textural effects, such as ice-ice bonding, clustering strength of c-axes and anisotropic geometry of pore space and ice, as a function of textural components within firn.
(2) Quantify softening/hardening effects by Cl^-, F^- and NH_4^+ ions in terms of concentration, temperature and ion balance.
(3) Re-examine firn densification models, because no models have yet considered the textural effects, the softening/hardening effects of Cl^-, F^- and NH_4^+ ions, or the dimension of $\Delta\varepsilon$. The basic components of the firn densification model relate the driving force and the rate of densification as a function of temperature (e.g. Cuffey and Paterson, 2010). Based on the present study, we must consider the counterclockwise rotation process of data distribution in the $\Delta\varepsilon$–ε_h space (geometrical anisotropy-density space) caused by the textural effects. These problems are important in order to properly model the gas enclosure process within the ice sheet.
(4) Explore the depositional environment at the surface of the ice sheet at the ice coring sites, in order to better understand the roles of the accumulation rate, temperature, temperature gradient, wind, formation of frost, redeposition and summer insolation.

Finally, microwave remote sensing of polar ice sheets is a research field in which we use knowledge in the evolution and spatial variability of ε_h, ε_v and $\Delta\varepsilon$. The data presented herein are important in clarifying the signals of microwave remote sensors. For nadir propagation of the electromagnetic waves, we should use only ε_h. However, when oblique incidence is used, all components of ε_h, ε_v and $\Delta\varepsilon$ are necessary for analysis of both wave propagation and reflections. These topics should be explored in the future.

AUTHOR CONTRIBUTION STATEMENT

S. Fujita headed the present study, performed basic measurements such as dielectric permittivity measurements of firn, performed basic analyses and wrote the paper. H. Motoyama headed the ice core drilling, performed basic measurements and logging, and transportation of the cores from Antarctica to Japan. K. Goto-Azuma and M. Hirabayashi headed the analyses of major ions and water stable isotope ratios at NIPR. A. Hori and Y. Iizuka headed the basic analyses of the DF99 core in ILTS. Y. Motizuki and K. Takahashi headed the analyses of the DFS10 core for major ions at RIKEN. A. Hori and S. Fujita measured the density profile of the DFS10 core. All of the authors joined in the discussions while preparing the paper.

ACKNOWLEDGEMENTS

The present research was supported by Grants-in-Aid for Scientific Research (A) (20201007) and (A) (20241007) from the Japan Society for the Promotion of Science (JSPS). Support from DF project field members and the laboratory technicians at NIPR is appreciated. The writing of the present paper was supported by an NIPR publication subsidy. The paper was much improved thanks to thoughtful comments provided by T. Kobashi, T. Hondoh, two anonymous reviewers and S.H. Faria as scientific editor.

REFERENCES

Alley RB (1988) Concerning the deposition and diagenesis of strata in polar firn. *J. Glaciol.*, **34**(118), 283–290

Anderson DL and Benson CS (1963) The densification and diagenesis of snow. In Kingery WD ed. *Ice and snow: properties, processes, and applications*. MIT Press, Cambridge, MA, 391–411

Bader H (1939) Mineralogische und strukturelle Charakterisierung des Schnees und seiner Metamorphose. In Bader H and 6 others eds *Der Schnee und seine Metamorphose* (Beiträge zur Geologie der Schweiz, Geotechnische Serie Hydrologie 3), 1–61 [Transl. Tienhaven JCV (1954), Snow and its metamorphism, SIPRE Transl. 14, 1–55]

Bamber JL, Gomez-Dans JL and Griggs JA (2009) *Antarctic 1 km Digital Elevation Model (DEM) from Combined ERS-1 Radar and ICES at Laser Satellite Altimetry*. National Snow and Ice Data Center, Digital media, Boulder, Colorado, USA

Barnes PRF and 5 others (2003) Evolution of chemical peak shapes in the Dome C, Antarctica, ice core. *J. Geophys. Res.*, **108**(D3), 4126

Bazin L and 21 others (2012) An optimized multi-proxy, multi-site Antarctic ice and gas orbital chronology (AICC2012): 120–800 ka. *Clim. Past*, **9**(4), 1715–1731 (doi: 10.5194/cp-9-1715-2013)

Bender ML (2002) Orbital tuning chronology for the Vostok climate record supported by trapped gas composition. *Earth Planet. Sci. Lett.*, **204**(1–2), 275–289 (doi: 10.1016/S0012-821X(02)00980-9)

Benson CS (1962) Stratigraphic studies in the snow and firn of the Greenland ice sheet. *SIPRE Res. Rep.*, **70**, 76–83

Colbeck SC (1989) Snow-crystal growth with varying surface temperatures and radiation penetration. *J. Glaciol.*, **35**(119), 23–29 (doi: 10.3189/002214389793701536)

Craven M and Allison I (1998) Firnification and the effects of windpacking on Antarctic snow. *Ann. Glaciol.*, **27**, 239–245

Cuffey KM and Paterson WSB (2010) *The physics of glaciers*, 4th edn. Butterworth-Heinemann, Oxford

Dang H, Genthon C and Martin E (1997) Numerical modeling of snow cover over polar ice sheets. *Ann. Glaciol.*, **25**, 170–176

Evans S (1965) Dielectric properties of ice and snow-a review. *J. Glaciol.*, **5**(42), 773–792

Freitag J, Wilhelms F and Kipfstuhl S (2004) Microstructure dependent densification of polar firn derived from X-ray microtomography. *J. Glaciol.*, **50**(169), 243–250 (doi: 10.3189/172756504781830123)

Freitag J, Kipfstuhl S and Laepple T (2013) Core-scale radioscopic imaging: a new method reveals density–calcium link in Antarctic firn. *J. Glaciol.*, **59**(218), 1009–1014 (doi: 10.3189/2013JoG13J028)

Fujita S, Enomoto H, Kameda T, Motoyama H and Sugiyama S (2008) Changes of surface snow density in a summer in the Antarctic Dome Fuji region. *SCAR/IASC IPY Open Science Conference, July 8th-11th 2008*, St. Petersburg, Russia, Abstract Volume, 273–274

Fujita S, Okuyama J, Hori A and Hondoh T (2009) Metamorphism of stratified firn at Dome Fuji, Antarctica: a mechanism for local insolation modulation of gas transport conditions during bubble close off. *J. Geophys. Res.*, **114**(F3), F03023 (doi: 10.1029/2008JF001143)

Fujita S and 25 others (2011) Spatial and temporal variability of snow accumulation rate on the East Antarctic ice divide between Dome Fuji and EPICA DML. *Cryosphere*, **5**, 1057–1081 (doi: 10.5194/tc-5-1057-2011)

Fujita S and 7 others (2012) Radar diagnosis of the subglacial conditions in Dronning Maud Land, East Antarctica. *Cryosphere*, **6**(5), 1203–1219 (doi: 10.5194/tc-6-1203-2012)

Fujita S and 6 others (2014) Densification of layered firn of the ice sheet at NEEM, Greenland. *J. Glaciol.*, **60**(223), 905–921 (doi: 10.3189/2014JoG14J006)

Gerland S and 5 others (1999) Density log of a 181 m long ice core from Berkner Island, Antarctica. *Ann. Glaciol.*, **29**, 215–219 (doi: 10.3189/172756499781821427)

Gow AJ (1968) Deep core studies of the accumulation and densification of snow at Byrd Station and Little America V, Antarctica. *CRREL Res. Rep.*, **197**

Gow AJ (1975) Time–temperature dependence of sintering in perennial isothermal snowpacks. IAHS Publ. 114 (Symposium at Grindelwald 1974 – *Snow Mechanics*), 25–41

Hondoh T (2000) Firn densification, close-off and air bubbles. In Hondoh T ed. *Physics of ice core records*. Hokkaido University Press, Sapporo, 283–359

Hörhold MW, Kipfstuhl S, Wilhelms F, Freitag J and Frenzel A (2011) The densification of layered polar firn. *J. Geophys. Res.*, **116**(F1), F01001 (doi: 10.1029/2009JF001630)

Hörhold MW and 5 others (2012) On the impact of impurities on the densification of polar firn. *Earth Planet. Sci. Lett.*, **325–326**, 93–99 (doi: 10.1016/j.epsl.2011.12.022)

Hori A and 11 others (1999) A detailed density profile of the Dome Fuji (Antarctica) shallow ice core by X-ray transmission method. *Ann. Glaciol.*, **29**, 211–214 (doi: 10.3189/172756499781821157)

Hoshina Y and 8 others (2014) Effect of accumulation rate on water stable isotopes of near-surface snow in inland Antarctica. *J. Geophys. Res. –Atmos.*, **119**(1), 274–283 (doi: 10.1002/2013jd020771)

Hutterli MA, Schneebeli M, Freitag J, Kipfstuhl J and Röthlisberger R (2009) Impact of local insolation on snow metamorphism and ice core records. *Low Temp. Sci., Ser. A, Data Rep.*, **68**, 223–232

Igarashi M, Kanamori N and Watanabe O (1998) Analytical method for small amount of polar snow and ice samples by ion chromatography (in Japanese with English abstract). *Antarct. Rec.*, **42**(1), 64–80

Igarashi M and 5 others (2011) Dating of the Dome Fuji shallow ice core based on a record of volcanic eruptions from AD 1260 to AD 2001. *Polar Sci.*, **5**(4), 411–420 (doi: 10.1016/j.polar.2011. 08.001)

Iizuka Y and 6 others (2004a) SO_4^{2-} minimum in summer snow layer at Dome Fuji, Antarctica, and the probable mechanism. *J. Geophys. Res.*, **109**, D04307 (doi: 10.1029/2003JD004138)

Iizuka Y, Takata M, Hondoh T and Fujii Y (2004b) High-time-resolution profiles of soluble ions in the last glacial period of a Dome Fuji (Antarctica) deep ice core. *Ann. Glaciol.*, **39**, 452–456 (doi: 10.3189/172756404781814302)

Iizuka Y, Hondoh T and Fujii Y (2006) Na_2SO_4 and $MgSO_4$ salts during the Holocene period derived by high-resolution depth analysis of a Dome Fuji ice core. *J. Glaciol.*, **52**(176), 58–64 (doi: 10.3189/172756506781828926)

Iizuka Y and 9 others (2012) The rates of sea salt sulfatization in the atmosphere and surface snow of inland Antarctica. *J. Geophys. Res.-Atmos.*, **117**, D04308 (doi: 10.1029/2011jd016378)

Johnsen SJ and 5 others (2000) Diffusion of stable isotopes in polar firn and ice: the isotope effect in firn diffusion. In Hondoh T. ed. *Physics of Ice Core Records*. Hokkaido University Press, Sapporo, 121–140

Jones RG (1976) Precise dielectric measurements at 35 GHz using an open microwave resonator. *Proc. IEEE*, **123**(4), 285–290 (doi: 10.1049/piee.1976.0067)

Jones SJ (1967) Softening of ice crystals by dissolved fluoride ions. *Phys. Lett. A*, **25**(5), 366–367 (doi: 10.1016/0375–9601(67)90702–5)

Jones SJ and Glen JW (1969) The effect of dissolved impurities on the mechanical properties of ice crystals. *Philos. Mag.*, **19**(157), 13–24 (doi: 10.1080/14786436908217758)

Kameda T, and 9 others (1997) Meteorological observations along a traverse route from coast to Dome Fuji Station, Antarctica, recorded by automatic weather station in 1995. *Proc. NIPR Symp. Polar Meteorol. Glaciol.*, **11**, 35–50

Kameda T, Motoyama H, Fujita S and Takahashi S (2008) Temporal and spatial variability of surface mass balance at Dome Fuji, East Antarctica, by the stake method from 1995 to 2006. *J. Glaciol.*, **54**(184), 107–116 (doi: 10.3189/002214308784409062)

Kawamura K and 5 others (2004) Close resemblance between local summer insolation, O_2/N_2 and total air content from the Dome Fuji Ice Core, Antarctica. *Eos*, **85**, Fall Meet. Suppl. [Abstr. C33C-0356]

Kawamura K and 17 others (2007) Northern hemisphere forcing of climatic cycles in Antarctica over the past 360,000 years. *Nature*, **448**(7156), 912–916 (doi: 10.1038/nature06015)

Kipfstuhl S and 8 others (2009) Evidence of dynamic recrystallization in polar firn. *J. Geophys. Res.*, **114**(B5), B05204 (doi: 10.1029/2008JB005583)

Koerner RM (1971) A stratigraphic method of determining the snow accumulation rate at Plateau Station, Antarctica, and application to South Pole-Queen Maud Land Traverse 2, 1965–1966. In Crary AP, ed. *Antarctic ice studies II*, American Geophysical Union, Washington, DC, 225–238

Komiyama B (1991) Open resonator for precision dielectric measurements in the 100 GHz band. *IEEE Trans. Microw. Theory Tech.*, **39**(10), 1792–1796 (doi: 10.1109/22.88556)

Landais A and 11 others (2012) Towards orbital dating of the EPICA Dome C ice core using $\delta O_2/N_2$. *Clim. Past*, **8**(1), 191–203 (doi: 10.5194/cp-8-191-2012)

Livingston FE and George SM (2002) Effect of sodium on HCl hydrate diffusion in ice: evidence for anion-cation trapping. *J. Phys. Chem. A*, **106**(20), 5114–5119 (doi: 10.1021/jp0145309)

Lomonaco R, Albert MR and Baker I (2011) Microstructural evolution of fine-grained layers through the firn column at Summit, Greenland. *J. Glaciol.*, **57**(204), 755–762 (doi: 10.3189/002214311797409730)

Lytle VI and Jezek KC (1994) Dielectric permittivity and scattering measurements of Greenland firn at 26.5–40 GHz. *IEEE Trans. Geosci. Remote Sens.*, **32**(2), 290–295 (doi: 10.1109/36.295044)

Maeno N and Ebinuma T (1983) Pressure sintering of ice and its implication to the densification of snow at polar glaciers and ice sheets. *J. Phys. Chem.*, **87**(21), 4103–4110 (doi: 10.1021/j100244a023)

Matsuoka T, Fujita S, Morishima S and Mae S (1997) Precise measurement of dielectric anisotropy in ice Ih at 39 GHz. *J. Appl. Phys.*, **81**(5), 2344–2348 (doi: 10.1063/1.364238)

Miyashita H (2008) The new high precision gamma-ray density meter PH-1000: certificated by MEXT. *Jpn. Tappi J.*, **62**(3), 309–312

Nakamura T and Jones SJ (1970) Softening effect of dissolved hydrogen chloride in ice crystals. *Scripta Metall.*, **4**(2), 123–126

Raynaud D and 5 others (2007) The local insolation signature of air content in Antarctic ice: a new step toward an absolute dating of ice records. *Earth Planet. Sci. Lett.*, **261**(3–4), 337–349 (doi: 10.1016/j.epsl.2007.06.025)

Röthlisberger R and 8 others (2003) Limited dechlorination of sea-salt aerosols during the last glacial period: evidence from the European Project for Ice Coring in Antarctica (EPICA) Dome C ice core. *J. Geophys. Res.*, **108**(D16), 4526 (doi: 10.1029/2003jd003604)

Shiraiwa T, Shoji H, Saito T, Yokoyama K and Watanabe O (1996) Structure and dielectric properties of surface snow along the traverse route from coast to Dome Fuji Station, Queen Maud Land, Antarctica. *Proc. NIPR Symp. Polar Meteorol. Glaciol.*, **10**, 1–12

Sihvola A and Kong J (1988) Effective permittivity of dielectric mixtures. *IEEE Trans. Geosci. Remote Sens.*, **26**(4), 420–429 (doi: 10.1109/36.3045)

Sugiyama S and 6 others (2012) Snow density along the route traversed in the Japanese-Swedish Antarctic Expedition, 2007/08. *J. Glaciol.*, **58**(209), 529–539 (doi: 10.3189/2012JoG11J201)

Suwa M and Bender ML (2008a) O_2/N_2 ratios of occluded air in the GISP2 ice core. *J. Geophys. Res.*, **113**(D11), D11119 (doi: 10.1029/2007JD009589)

Suwa M and Bender ML (2008b) Chronology of the Vostok ice core constrained by O_2/N_2 ratios of occluded air, and its implication for the Vostok climate records. *Quat. Sci. Rev.*, **27**(11–12), 1093–1106 (doi: 10.1016/j.quascirev.2008.02.017)

Thibert E and Domine F (1997) Thermodynamics and kinetics of the solid solution of HCl in ice. *J. Phys. Chem. B*, **101**(18), 3554–3565 (doi: 10.1021/jp962115o)

Watanabe O, and 12 others (1997) Preliminary discussion of physical properties of the Dome Fuji shallow ice core in 1993, Antarctica. *Proc. NIPR Symp. Polar Meteorol. Glaciol.*, **11**, 1–8

Watanabe O and 5 others (2003) Homogeneous climate variability across East Antarctica over the past three glacial cycles. *Nature*, **422**, 509–512 (doi: 10.1038/nature01525)

APPENDIX

Table A8. Facts, explanations and related notes for the densification of polar firn

ID	Facts and references	Proposed explanations for the facts	Status of the explanation, support or objections, and/or related notes
1	Preferential deformation of initially low density firn, compared with the initial high density firn, or in other words, density crossover. (Gerland and others, 1999; Freitag and others, 2004; Fujita and others, 2009, 2014; Hörhold and others, 2011, 2012, and this study)	Textural effects such as ice–ice bonding, additional clustering of *c*-axes around the vertical, and anisotropic geometry of ice and pore spaces (Fujita and others, 2009)	Hypothesized by Fujita and others (2009). Hörhold and others (2011) noted "*a firn core study including high-resolution profiles of chemistry, microstructure and density is strongly needed*. Hörhold and others (2012) noted "*A well-tested explanation, supported by detailed data comparison of density of layers from the near surface to layers from greater depths, is still lacking*"
2	Evolution of positive correlation between densification and Na^+ concentrations and Cl^- concentrations. (Fujita and others, 2014; this study)	Softening effects of ice as a result of the presence of Cl^- in the lattice of ice crystal. Presence of Cl^- at the crystal lattice of ice causes modulation of movement and amount of dislocations. (Fujita and others, 2014; this study.)	Softening/hardening effects by F^-, Cl^- and NH_4^+ were empirically known for single crystals (Jones, 1967; Jones and Glen, 1969; Nakamura and Jones, 1970). Cuffey and Paterson (2010) noted "*for the ice sheets, no convincing evidence suggests a quantitatively significant direct effect of soluble impurities*"
3	Empirical correlation between deformation and some ions such as Ca^{2+} at sites in Greenland and at some sites in Antarctica. (Hörhold and others, 2012; Freitag and others, 2013)	Hörhold and others (2012) noted as follows.(1) "*Polar firn impurities consist of soluble contents and microparticles and both can be thought to alter the density of the firn*" (2) "*Alternatively, the impurity content in terms of particulate dust is assumed to be localized at the grain boundaries and triple junctions. It may therefore increase the thickness of the quasi-liquid layer coating of individual grains*"	Fujita and others (2014) noted that no evidence supported the explanation. Fujita and others (2014) hypothesized that the layered deformation is combined effects of the textural effects initially formed by the seasonal variation of metamorphism and a result of ions such as F^-, Cl^- and NH_4^+. They further hypothesized that high correlations between Ca^{2+} ions and deformation are superficially caused by the seasonal synchronicity with cycles of F^-, Cl^- and NH_4^+ and the seasonal variation of metamorphism
4	Evolution of positive correlation between densification and F^-, Cl^- and cations concentrations in Greenland NEEM firn (Fujita and others, 2014)	Same explanation as ID 2 above. Softening effects of ice as a result of the presence of F^- and/or Cl^- in the lattice of ice crystal	Same status as ID 2 above

MS received 28 January 2015 and accepted in revised form 15 October 2015; first published online 21 March 2016)